Interactions between tropospheric chemistry and aerosols in a unified general circulation model

Hong Liao, Peter J. Adams, Serena H. Chung, and John H. Seinfeld

Division of Engineering and Applied Science and Department of Chemical Engineering, California Institute of Technology, Pasadena, California, USA

Loretta J. Mickley and Daniel J. Jacob

Department of Earth and Planetary Sciences and Division of Engineering and Applied Sciences, Harvard University, Cambridge, Massachusetts, USA

Received 29 August 2001; revised 8 March 2002; accepted 15 May 2002; published 2 January 2003.

[1] A unified tropospheric chemistry-aerosol model has been developed within the Goddard Institute for Space Studies general circulation model (GCM). The model includes a detailed simulation of tropospheric ozone-NO_x-hydrocarbon chemistry as well as aerosols and aerosol precursors. Predicted aerosol species include sulfate, nitrate, ammonium, black carbon, primary organic carbon, and secondary organic carbon. The partitioning of ammonia and nitrate between gas and aerosol phases is determined by on-line thermodynamic equilibrium, and the formation of secondary organic aerosols is based on equilibrium partitioning and experimentally determined parameters. Two-way coupling between aerosols and chemistry provides consistent chemical fields for aerosol dynamics and aerosol mass for heterogeneous processes and calculations of gas-phase photolysis rates. Although the current version of the unified model does not include a prognostic treatment of mineral dust, we include its effects on photolysis and heterogeneous processes by using three-dimensional off-line fields. We also simulate sulfate and nitrate aerosols that are associated with mineral dust based on currently available chemical understanding. Considering both mineral dust uptake of HNO_3 and wet scavenging of HNO_3 on ice leads to closer agreement between predicted gas-phase HNO_3 concentrations and measurements than in previous global chemical transport model simulations, especially in the middle to upper troposphere. As a result of the coupling between chemistry and aerosols, global burdens of both gas-phase and aerosol species are predicted to respond nonlinearly to changing emissions of NO_x, NH_3, and sulfur. *INDEX TERMS:* 0365 Atmospheric Composition and Structure: Troposphere—composition and chemistry; 1610 Global Change: Atmosphere (0315, 0325); 0305 Atmospheric Composition and Structure: Aerosols and particles (0345, 4801); *KEYWORDS:* ozone, aerosols, atmospheric chemistry

Citation: Liao, H., P. J. Adams, S. H. Chung, J. H. Seinfeld, L. J. Mickley, and D. J. Jacob, Interactions between tropospheric chemistry and aerosols in a unified general circulation model, *J. Geophys. Res.*, *108*(D1), 4001, doi:10.1029/2001JD001260, 2003.

1. Introduction

[2] Tropospheric O_3 and aerosols are controlled by a combination of direct and precursor emissions, chemical reactions in the atmosphere, and meteorological processes, each of which has the potential to be affected by climate change with resulting feedbacks. Better understanding of chemistry-aerosol-climate interactions is needed for assessments of future climate change [*National Research Council*, 2001].

[3] A fully coupled chemistry-aerosol-climate model, a so-called unified model, will allow one to address how changes in emissions will affect future abundances of tropospheric O_3, CH_4, and aerosols over the next century. Understanding of chemistry-aerosol-climate interactions is complicated by the many feedbacks from climate change to tropospheric chemistry and aerosols. For example, changes in the atmospheric water cycle affect O_3 photochemistry [*Johnson*, 1999] as well as the formation, optical properties, cloud activating properties, and wet scavenging of aerosols. Changes in tropospheric circulation affect the distributions and hence the radiative forcing of O_3 and aerosols [*Hansen et al.*, 1997]. Changes in stratospheric circulation affect stratosphere-troposphere exchange of O_3 and also modify the UV actinic flux in the troposphere. Rising temperatures affect emissions of NO_x, hydrocarbons, and ammonia [*Yienger and Levy*, 1995; *Guenther et al.*, 1995; *Bouwman et al.*, 1997]. Increasing deep convection enhances the lightning source of NO_x [*Sinha and Toumi*, 1997; *Toumi et al.*, 1996]. Increasing sea surface winds promote emissions of dimethylsulfide (DMS) and sea salt aerosol from the oceans [*Intergovernmental Panel on Climate Change* (*IPCC*), 2001].

0148-0227/03/2001JD001260$09.00

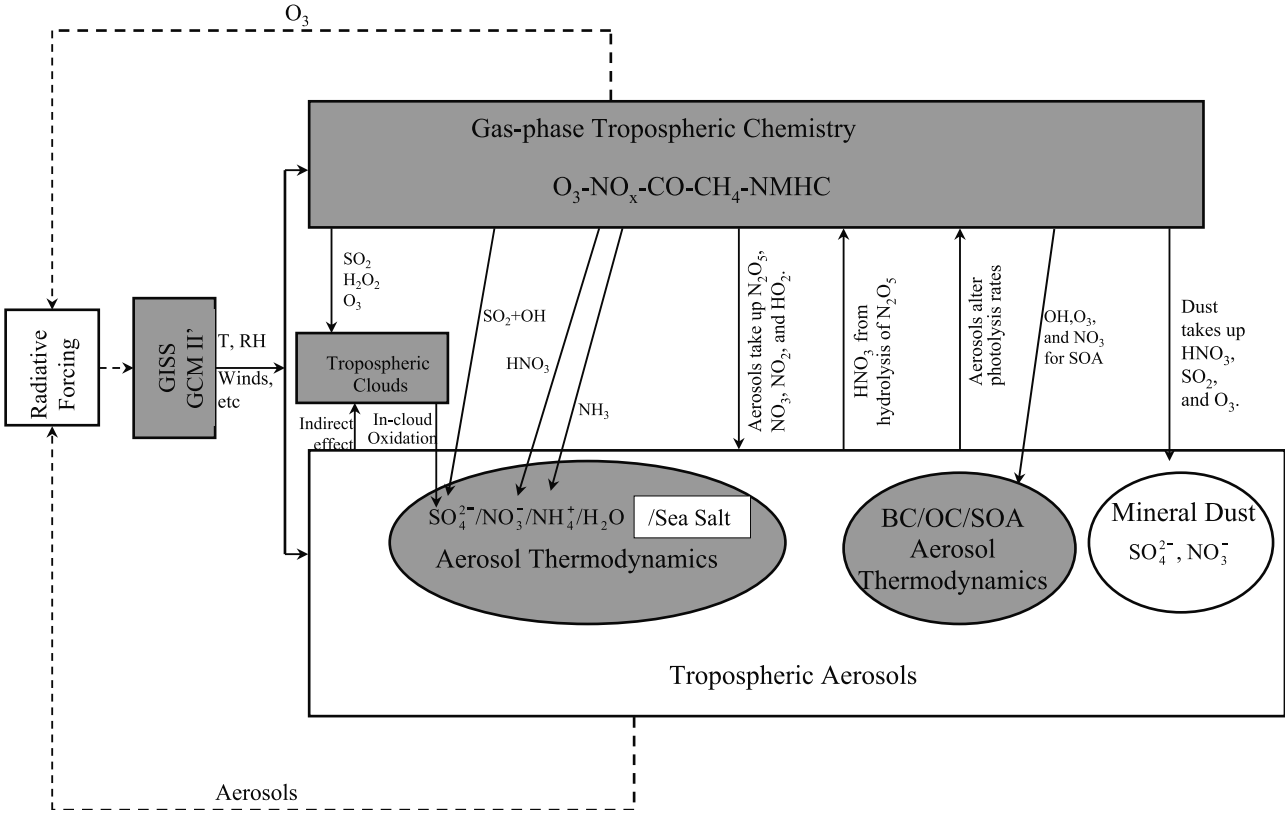

Figure 1. Structure of the GCM-atmospheric chemistry-aerosol-climate coupled model. Shaded components and interactions indicated by solid lines are included in the current work. Off-line fields of mineral dust are used for simulations of heterogeneous reactions and photolysis rates. Sea salt aerosol is not included in the current work.

[4] Over the past two decades, global simulations of O_3 and aerosols have evolved from using archived meteorological fields in chemical transport models (CTMs) to on-line simulations within general circulation models (GCMs) that have the potential to account for correlations among chemical, aerosol, and meteorological variables. Tropospheric O_3 chemistry has been modeled in GCMs by *Roelofs and Lelieveld* [1995, 2000], *Roelofs et al.* [1997], *Mickley et al.* [1999], and *Shindell et al.* [2001]. GCM simulations of sulfate [*Feichter et al.*, 1996; *Lelieveld et al.*, 1997; *Kjellstrom*, 1998; *Roelofs et al.*, 1998; *Koch et al.*, 1999; *Lohmann et al.*, 1999; *Adams et al.*, 1999, 2001; *Barth et al.*, 2000; *Koch*, 2001], biomass burning and/or black carbon (BC) [*Cooke et al.*, 1999; *Koch*, 2001], nitrate [*Adams et al.*, 1999, 2001], ammonium [*Adams et al.*, 1999, 2001], and mineral dust [*Tegen and Miller*, 1998; *Woodward*, 2001] have been reported. However, most previous GCM simulations considered gas-phase chemistry and aerosols separately. *Roelofs et al.* [1998] considered coupling between tropospheric chemistry and sulfate aerosol within a GCM but did not systematically examine the interactions between gas-phase chemistry and aerosols.

[5] While concentrations of gas-phase species govern many aspects of the formation and growth of aerosols, particles, in turn, influence gas-phase atmospheric chemistry by altering photolysis rates [*Demerjian et al.*, 1980; *Ruggaber et al.*, 1994; *Lantz et al.*, 1996; *Castro et al.*, 1997; *Landgraf and Crutzen*, 1998; *Dickerson et al.*, 1997; *Jacobson*, 1998; *Liao et al.*, 1999] and by serving as sites for heterogeneous conversion of gas-phase species [*Dentener and Crutzen*, 1993; *Andreae and Crutzen*, 1997]. Previous on-line tropospheric chemistry (aerosol) models generally used off-line aerosol (gas-phase species) fields. For example, concentrations of OH, NO_3, HO_2, or O_3 required in sulfate aerosol simulations have been imported from off-line atmospheric chemistry models [*Feichter et al.*, 1996; *Koch et al.*, 1999; *Adams et al.*, 1999; *Barth et al.*, 2000], and off-line aerosol concentrations have been used in global chemistry models to simulate heterogeneous processes [*Brasseur et al.*, 1998; *Wang et al.*, 1998; *Mickley et al.*, 1999]. Off-line fields cannot account for two-way interactions between tropospheric chemistry and aerosols, which are desired in simulations when climate changes feed back into gas-phase chemistry and aerosols.

[6] To move toward incorporating interactions and feedbacks among tropospheric chemistry, aerosol formation, and climate change in a GCM, we report here the development of a unified model that simulates atmospheric chemistry and sulfate/nitrate/ammonium, BC, primary organic aerosol (POA), and secondary organic aerosol (SOA) on-line in the Goddard Institute for Space Studies (GISS) GCM version II prime. This work represents the first phase of the development of the fully coupled model depicted schematically in Figure 1. Full simulation of tropospheric chemistry provides consistent chemical fields for aerosol dynamics, including OH, H_2O_2, and O_3 for sulfate forma-

Table 1. GCM Variables Passed to Tropospheric Chemistry and Aerosol Modules

GCM Variables	For Computations of
Frequency and amount of precipitation	soil NO_x emissions; wet deposition
Frequency of convective events	lightning NO_x emissions
Boundary layer height	dry deposition
Surface wind velocity	dry deposition; DMS emission
Surface albedo	dry deposition
Cloud optical depth	dry deposition; isoprene emission flux; photolysis rates
Temperature	reaction rates; dry deposition; photolysis rates; aerosol thermodynamic equilibrium
Relative humidity	reaction rates; aerosol thermodynamic equilibrium
Air pressure	reaction rates; photolysis rates
Cloud volume fraction	in-cloud sulfate formation; wet deposition

tion, HNO_3 for nitrate formation, NH_3 for ammonium formation, and OH, O_3, and NO_3 for SOA formation; in turn, the model provides consistent aerosol fields for simulations of heterogeneous processes and gas-phase photolysis rates. Although the version of the unified model presented here does not include prognostic calculation of mineral dust aerosol, we include its effects on photolysis rates and heterogeneous reactions by using three-dimensional monthly mean fields. Sea salt aerosol is not included in the current model. The unified model includes the tropospheric chemical mechanism developed by *Mickley et al.* [1999], the thermodynamic representation of sulfate/nitrate/ammonium aerosols of *Adams et al.* [1999, 2001], and the carbonaceous aerosol simulation of *Chung and Seinfeld* [2002].

[7] We describe the coupled GCM-atmospheric chemistry-aerosol model in section 2, and discuss emission inventories in section 3. Section 4 presents simulated concentrations of aerosols and related gas-phase species. We discuss the important processes that affect gas-phase HNO_3 concentrations in section 5. In section 6, we examine the effect of aerosols on gas-phase photolysis, and in section 7, we investigate the effects of heterogeneous reactions on predicted concentrations of gas-phase and aerosol species. Section 8 addresses the sensitivity of predicted concentrations to emissions of NO_x, NH_3, and sulfur.

2. Unified Model

[8] The unified model consists of three major components: (1) the Goddard Institute for Space Studies GCM II-prime (GISS GCM II'); (2) the Harvard tropospheric O_3-NO_x-hydrocarbon chemical mechanism [*Mickley et al.*, 1999, and references therein] that uses the Fast-J scheme developed by *Wild et al.* [2000] for the calculation of atmospheric photolysis rates; (3) the aerosol thermodynamic equilibrium model ISORROPIA [*Nenes et al.*, 1998] for computing the local equilibrium of the aerosol sulfate/nitrate/ammonium/water system, and equilibrium computation of SOA formation [*Hoffmann et al.*, 1997; *Griffin et al.*, 1999b].

2.1. GISS GCM II'

[9] The GISS GCM II', as described by *Rind and Lerner* [1996] and by *Rind et al.* [1999], has a resolution of 4° latitude by 5° longitude, with nine vertical layers in a σ-coordinate system extending from the surface to 10 mbar. In comparison with the original GISS GCM II [*Hansen et al.*, 1983], this version has improved treatments of the boundary layer, convection, land surface, and cloud liquid water budget [*Rind and Lerner*, 1996]. The version of GISS GCM II' used in this study employs monthly mean ocean temperature maps. The dynamical time step is 1 hour. The variables passed from GISS GCM II' to the tropospheric chemistry and aerosol modules are listed in Table 1.

2.2. Tropospheric Chemistry

[10] The gas-phase tropospheric chemical mechanism represents tropospheric O_3-NO_x-hydrocarbon chemistry based on 110 chemical species (24 tracers) and 305 chemical reactions. The chemistry subroutines are called every 4 hours, and the chemical mechanism is integrated with a fast Gear solver [*Jacobson and Turco*, 1994]. Gas-phase chemical reactions added to the Harvard mechanism to account for sulfate, nitrate, and SOA formation are listed in Table 2. In addition to the 24 tracers included in the model described by *Mickley et al.* [1999], 43 tracers are added for aerosols. The suite of tracers transported in

Table 2. Additional Gas-Phase Chemical Reactions Related to Sulfate, Nitrate, and Carbonaceous Aerosols

Reaction	Rate Coefficient (cm^3 $molecule^{-1}s^{-1}$)	Reference
$DMS + OH \rightarrow 0.75\ SO_2 + 0.25\ MSA$	$\frac{1.7\times10^{-42}\exp(7810/T)[O_2]}{1+5.5\times10^{-31}\exp(7460/T)[O_2]}$	*Chin et al.* [1996]
$DMS + OH \rightarrow SO_2$	$9.6 \times 10^{-12}\ \exp(-234/T)$	*Chin et al.* [1996]
$DMS + NO_3 \rightarrow HNO_3 + SO_2$	$1.9 \times 10^{-13}\ \exp(520/T)$	*Atkinson et al.* [1992]
$SO_2 + OH + M \rightarrow H_2SO_4 + M$	$\left(\frac{k_0(T)}{1+k_0(T)/k_\infty}\right)F_c\{1 + [\log_{10}(k_0(T)/k_\infty)]^2\}^{-1}$ [a]	*Atkinson et al.* [1992]
$NH_3 + OH \rightarrow NH_2 + H_2O$	$1.7 \times 10^{-12}\ \exp(-710\ /T)$	*DeMore et al.* [1997]
$HC_i + OX_j \rightarrow \alpha_{i,j,1}G_{i,j,1} + \alpha_{i,j,2}G_{i,j,2} + \ldots$ [b]	different for each hydrocarbon class	*Chung and Seinfeld* [2002]

[a] In this equation, $k_0(T) = 4.0 \times 10^{-31}(T/300)^{-3.3}[M]$, $k_\infty = 2 \times 10^{-12}$, $F_c = 0.45$.

[b] HC_i represents hydrocarbon class i. Reactive hydrocarbons are grouped into five categories according to the values of their experimentally measured aerosol yield parameters [*Griffin et al.*, 1999a, 1999b], see Table 3 for the composition of each class. OX_j is either OH, O_3, or NO_3, $\alpha_{i,j,k}$ s are mass-based stoichiometric coefficients given by *Griffin et al.* [1999a, 1999b], and $G_{i,j,k}$ s are the semi-volatile products.

the GISS GCM II' is listed in Table 3, in which SO_2, SO_4^{2-}, DMS, NH_3, NH_4^+, and NO_3^- are those used for the simulation of $SO_4^{2-}/NO_3^-/NH_4^+$ aerosol, and 37 are used for the simulation of carbonaceous aerosols: hydrophobic BC, hydrophilic BC, hydrophobic POA, hydrophilic POA, five classes of parent hydrocarbons, as well as 14 gas-phase and 14 aerosol-phase products produced when parent hydrocarbons are oxidized by O_3, OH, and NO_3. The last 28 tracers are needed because for each of the first four classes of parent hydrocarbons listed in Table 3, there are three oxidation products, two for combined O_3 and OH oxidation and one for NO_3 oxidation. In the case of sesquiterpenes, only two products are required (one for combined O_3 and OH oxidation and one for NO_3 oxidation) [*Griffin et al.*, 1999a, 1999b]. These oxidation products are semi-volatile and partition between the gas and aerosol phases; hence each product requires two tracers, making a total of 28 tracers for oxidation products.

2.2.1. Aqueous-Phase SO_2 Oxidation

[11] Reaction rates and equilibria for aqueous-phase oxidation of SO_2 by H_2O_2 and O_3 are given in Table 4. Note that oxidation by O_3 is very sensitive to pH. To compute rates of oxidation, cloud droplet pH is determined based on electroneutrality: $[H^+] = [HSO_3^-] + 2[SO_4^{2-}] + [NO_3^-] - [NH_4^+]$. H_2O_2 and O_3 fields for each grid cell and at each time step are predicted directly from the tropospheric chemistry. To account for changes of pH and aqueous-phase concentrations of H_2O_2 and SO_2 that occur over short timescales, as shown by *Barth et al.* [2000], aqueous-phase chemistry is integrated independently using a 4-min time step.

[12] It should be noted that mineral dust and associated sulfate and nitrate are assumed not to affect cloud pH. This may be an acceptable assumption because the main concentrations of clouds are not over dust source regions. A limitation of the pH calculation is the lack of inclusion of organic acids. We expect to overestimate cloud pH wherever concentrations of organic acids are high.

2.2.2. Aerosol Equilibrium

[13] Volatile atmospheric species tend to partition themselves between gas and aerosol phases in accordance with thermodynamic equilibrium [*Seinfeld and Pandis*, 1998]. As used by *Adams et al.* [1999], the thermodynamic equilibrium model ISORROPIA [*Nenes et al.*, 1998] is employed to simulate the partitioning of ammonia, nitric acid, and water between gas and aerosol phases. At relative humidity (RH) <100%, ISORROPIA computes the equilibrium composition of an internally mixed aerosol consisting of sulfate, nitrate, chloride, ammonium, sodium, and water. (Sodium and chloride are not considered in the present study.) For the $SO_4^{2-}/NO_3^-/NH_4^+/H_2O$ system, the inputs needed by ISORROPIA are the total concentrations of $NH_3 + NH_4^+$, $HNO_3 + NO_3^-$, and SO_4^{2-}, which are not associated with mineral dust, together with the ambient relative humidity and temperature. As discussed in *Adams et al.* [1999], we assume that aerosol particles exist in a hydrated, metastable state between their crystallization and deliquescence humidities.

[14] For SOA formation, the semi-volatile reaction products from reactions of parent hydrocarbons with OH, O_3, and NO_3 partition between the gas and aerosol phases. The fraction of each product that partitions to the aerosol phase is governed by an equilibrium partition coefficient $K_{om,i,j,k}$ [*Pankow*, 1994a, 1994b]

$$[G]_{i,j,k} = \frac{[A]_{i,j,k}}{K_{om,i,j,k}\, M_o} \tag{1}$$

where $[G]_{i,j,k}$ is the k^{th} gas-phase product from the reaction of hydrocarbon class i with oxidant j, $[A]_{i,j,k}$ is the product concentration in the aerosol phase, and M_o is the total concentration of organic aerosol, i.e.

$$M_o = [POA] + \sum_{i,j,k} [A]_{i,j,k} \tag{2}$$

where [POA] is the concentration of POA. The partitioning coefficients are temperature dependent and are given by *Griffin et al.* [1999a, 1999b] and *Chung and Seinfeld* [2002].

Table 3. GCM Chemical Tracers

Tracers	Composition
O_x	$O_3 + O + NO_2 + 2 \times NO_3$
NO_x	$NO + NO_2 + NO_3 + HNO_2$
HNO_3	
HNO_4	
N_2O_5	
PAN	peroxyacetyl nitrate
H_2O_2	
CO	
C_3H_8	
C_2H_6	
ALK4	lumped $\geq C_4$ alkanes
PRPE	lumped $\geq C_3$ alkenes
Isoprene	
Acetone	
CH_3OOH	
CH_2O	
CH_3CHO	
RCHO	lumped $\geq C_3$ aldehydes
MEK	lumped $\geq C_4$ ketones
Methyl vinyl ketone	
Methacrolein	
MPAN	peroxymethacryloyl nitrate
PPN	lumped peroxyacyl nitrates
R4N2	lumped alkyl nitrates
SO_2	
SO_4^{2-}	
DMS	
NH_3	
NH_4^+	
NO_3^-	
Hydrophobic BC	
Hydrophilic BC	
Hydrophobic POA	
Hydrophilic POA	
Hydrocarbon I	α-pinene, β-pinene, sabinene, Δ^3-carene, terpenoid ketones
Hydrocarbon II	limonene
Hydrocarbon III	α-terpinene, γ-terpinene, terpinolene
Hydrocarbon IV	myrcene, terpenoid alcohols, ocimene
Hydrocarbon V	sesquiterpenes
14 Gas-phase products	from reactions of hydrocarbon classes I to V with OH, O_3, NO_3
14 Aerosol-phase products	from gas-aerosol partitioning of 14 gas-phase products

2.2.3. Heterogeneous Reactions

[15] Hydrolysis of N_2O_5 on wetted surfaces of $SO_4^{2-}/NO_3^-/NH_4^+/H_2O$, POA, SOA, and mineral dust aerosols is included, and the HNO_3 produced equilibrates between the

Table 4. Aqueous Reactions Involved In-Cloud Production of Sulfate

	Reaction	k_{298}[a]	E/R	Reference
	Aqueous Chemistry			
(R1)	$HSO_3^- + H_2O_2 \rightarrow SO_4^{2-} + 2H^+ + H_2O$	7.45×10^7[b]	4759	*Jacob* [1986]
(R2)	$HSO_3^- + O_3 \rightarrow SO_4^{2-} + H^+ + O$	3.7×10^5	5300	*Barth et al.* [2000]
(R3)	$SO_3^2 + O_3 \rightarrow SO_4^{2-} + O_2$	1.5×10^9	5280	*Barth et al.* [2000]
	Equilibria			
(R4)	$H_2O_2 \Longleftrightarrow H_2O_2$ (aq)	7.4×10^4	−6643	*Jacob* [1986]
(R5)	$O_3 \Longleftrightarrow O_3$ (aq)	1.15×10^{-2}	−2560	*National Bureau of Standards* [1965]
(R6)	SO_2 (g) $\Longleftrightarrow SO_2$ (aq)	1.2	−3155	*Jacob* [1986]
(R7)	$H_2SO_3 \Longleftrightarrow HSO_3^- + H^+$	1.3×10^{-2}	−2015	*Maahs* [1982]
(R8)	$HSO_3 \Longleftrightarrow SO_3^{2-} + H^+$	6.3×10^{-8}	−1505	*Maahs* [1982]

[a]Units for second-order aqueous-phase reactions are M^{-1} s^{-1}. Units for solubility constants are M atm^{-1}. Units for dissociation constants are M. Reaction rates are of the form $k = k_{298}\exp[-(E/R)((1/T) - (1/298))]$ unless otherwise noted.
[b]$k = k_{298}\exp[-(E/R)((1/T) - (1/298))][H^+]$.

gas and aerosol phases. We also consider irreversible absorption of NO_3, NO_2, and HO_2 on wetted surfaces of $SO_4^{2-}/NO_3^-/NH_4^+/H_2O$, POA, SOA, and mineral dust aerosols. Despite the uncertainties associated with the uptake of SO_2, HNO_3, and O_3 by mineral dust [*Dentener et al.*, 1996], we include those heterogeneous reactions since studies have shown that these reactions are important to gas-phase chemistry [*Dentener et al.*, 1996; *Gay-Lacaux and Modi*, 1998; *Tabazadeh et al.*, 1998; *Song and Carmichael*, 2001; *Galy-Lacaux et al.*, 2001]. The first-order loss rate of a species on an aerosol surface is represented as shown by *Schwartz* [1986].

[16] Global, three-dimensional mass concentrations of $SO_4^{2-}/NO_3^-/NH_4^+/H_2O$, POA, and SOA aerosols are simulated. We use three-dimensional monthly mean fields of mineral dust from a different GISS GCM simulation [*Tegen and Fung*, 1994]. Mineral dust concentrations are the sum of both natural (undisturbed) and disturbed soils. BC is assumed not to participate in heterogeneous chemistry. Although we consider water associated with $SO_4^{2-}/NO_3^-/NH_4^+$ aerosol in the calculation of surface area, we do not consider water uptake by organic carbon (OC) and mineral dust. Sulfate, organic carbon (POA + SOA), and mineral dust aerosols are assumed to be externally mixed.

[17] For calculations of heterogeneous chemistry, aerosol size information is needed to obtain aerosol surface area concentration and surface mean radius. We assume a lognormal size distribution for dry $SO_4^{2-}/NO_3^-/NH_4^+$ particles with a median radius of 0.05 μm and geometric standard deviation of 2.0. In each grid cell, the ratio of wet to dry mass of $SO_4^{2-}/NO_3^-/NH_4^+$ aerosol is computed from thermodynamic equilibrium and is used to parameterize the size distribution of wet $SO_4^{2-}/NO_3^-/NH_4^+/H_2O$ aerosol as described by *Adams et al.* [2001]. We also assume a lognormal size distribution for each of OC and mineral dust aerosols, with a median radius of 0.0212 μm and a standard deviation of 2.24 for OC [*Cooke et al.*, 1999], and 0.88 μm and 1.7 for mineral dust [*Zhang and Carmichael*, 1999]. Densities are taken to be 1.8 g cm^{-3} for OC [*Cooke et al.*, 1999], and 2.6 g cm^{-3} for mineral dust [*Zhang and Carmichael*, 1999]. The density of $SO_4^{2-}/NO_3^-/NH_4^+/H_2O$ aerosol depends on its composition and is calculated as described by *Tang* [1997].

[18] The reaction probability γ is assumed to be 0.1, 0.001, 0.0001, and 0.2 for N_2O_5, NO_3, NO_2 and HO_2, respectively [*Jacob*, 2000]. For the uptake of SO_2, HNO_3 and O_3 by mineral dust aerosol, following *Dentener et al.* [1996], we use a reaction probability $\gamma(HNO_3)$ of 0.1, and $\gamma(SO_2)$ of 3×10^{-4} for regions with RH < 50% and $\gamma(SO_2)$ of 0.1 when RH > 50% [*Dentener et al.*, 1996]. $\gamma(O_3)$ is assumed to be 5×10^{-5} [*Dentener et al.*, 1996]. It should be noted that heterogeneous reactions on aerosols, especially those on mineral dust, are highly uncertain as little is known about reaction mechanisms and reaction rates [*Grassian*, 2001]. Mineral dust uptake may be influenced by temperature, relative humidity, and mass of dust. There is disagreement in the laboratory-determined reaction probability γ. For example, dry dust $\gamma(HNO_3)$ determined by *Fenter et al.* [1995] and *Hanisch and Crowley* [2001] was about one to two orders of magnitude greater than that determined by *Goodman et al.* [2000] and *Underwood et al.* [2001], and the uptake of HNO_3 increased by nearly a factor of 50 when RH was increased from near 0 to 16% [*Goodman et al.*, 2001]. Thus, while we use the best estimated values from previous studies to assess the potential role of heterogeneous reactions, these uncertainties should be kept in mind when evaluating model results.

[19] On mineral dust particles, deposited SO_2 and HNO_3 exist in the forms of SO_4^{2-} and NO_3^-, respectively. Since off-line mineral dust fields are used in this study, dust surface SO_4^{2-} and NO_3^- are predicted as diagnostic variables rather than tracers. It will turn out to be useful to separate sulfate that is not associated with mineral dust from that formed on mineral dust. Sulfate aerosol, which is emitted directly as primary particles, produced by gas-phase reaction of SO_2 with OH, or produced by in-cloud oxidation of SO_2 by H_2O_2 and O_3, will be denoted as SO_4^{2-}(*nondust*). Sulfate aerosol formed on mineral dust particles will be denoted as SO_4^{2-}(*dust*). Similarly, we denote nondust nitrate aerosol as NO_3^- (*nondust*), and nitrate that forms on mineral dust particles as NO_3^-(*dust*). *Dentener et al.* [1996] assumed that uptake of SO_2 and HNO_3 by mineral dust takes place only when the dust alkalinity exceeds the acidity from the dust-associated sulfate and nitrate. If alkalinity is contributed by the calcium ion, uptake of SO_2 and HNO_3 occurs when $[Ca^{2+}] - [SO_4^{2-}(dust)] - 0.5[NO_3^-(dust)] > 0$. We assume that the Ca^{2+} content of dust is 5% by weight [*Dentener et al.*, 1996].

[20] Off-line simulated global mineral dust concentrations by *Tegen and Fung* [1994] are used as a basis for calculat-

ing heterogeneous reactions. In order to calculate the dust alkalinity, it is necessary to account for the deposition of dust aerosol that contains sulfate and nitrate. Therefore, for each grid cell, we assume that the mass of dust deposited is simply balanced by an influx of fresh dust, and the fraction of SO_4^{2-}(*dust*) and NO_3^-(*dust*) deposited is the same as the fraction of deposited dust. We use monthly total (dry plus wet) deposition data (in kg m^{-2} $month^{-1}$) from *Tegen and Fung* [1995] and scale the total deposition at the surface to all grid cells above it by assuming that the deposition in a grid cell is proportional to the dust mass contained in it. It should be noted that by assuming in each grid cell the amount of fresh incoming dust is balanced by that deposited during a time step (in order to maintain a fixed global amount of dust), the change of dust alkalinity during transport is not accounted for. After emission, fresh dust particles take up SO_2 and HNO_3 as they are transported; thus, the alkalinity of dust particles in areas far away from source regions should be lower than that of freshly emitted dust particles. Our treatment of mineral dust has the effect of overestimating the dust-associated alkalinity in areas far away from dust sources while underestimating it in dust source regions. Consequently, this assumption may lead to an overestimation of the uptake of SO_2 and HNO_3 by dust removed from sources and an underestimation of uptake close to dust source regions. This treatment will also affect predicted vertical distributions of sulfate and nitrate that are associated with dust because of the assumed vertical distribution of dust deposition. More accurate simulation of dust uptake of gases requires treating both dust amount and dust alkalinity as prognostic tracers.

2.3. Gas-Phase Photolysis

[21] Rates of 40 photolysis reactions are computed every 4 hours using the Fast-J code of *Wild et al.* [2000], which accounts for absorption by O_2 and O_3, Rayleigh scattering, and Mie scattering by clouds and aerosols, using seven wavelength channels of varying widths covering the spectral range from 289 to 800 nm. We account for effects of SO_4^{2-}(*nondust*)/NO_3^-(*nondust*)/NH_4^+/H_2O, OC, BC, and mineral dust aerosols on photolysis rates. Predicted mass of SO_4^{2-}(*nondust*)/NO_3^-(*nondust*)/NH_4^+/H_2O, OC, and BC aerosols, as well as cloud optical depth, temperature, air pressure, surface albedo, and solar zenith angle from the GCM are passed to the Fast-J routine. Monthly mean fields of mineral dust aerosol are those used in the heterogeneous calculations (see section 2.2.1). Climatological O_3 distributions [*McPeters*, 1993] are used in Fast-J since most of the ozone column is in the stratosphere.

[22] Optical properties of clouds and aerosols are calculated by Mie theory [*Hansen and Travis*, 1974]. For temperatures equal to or exceeding 233 K, clouds diagnosed in GCM are assumed to be liquid, the scattering phase functions of which are calculated by assuming a Gamma distribution with constant $\alpha = 6$ and a mode radius of 8.0 μm [*Wild et al.*, 2000]. At temperatures less than 233 K, clouds are assumed to consist of irregular ice particles, with phase functions calculated following the method of *Mishchenko et al.* [1996]. For calculations of aerosol optical depth and phase functions, refractive indices for "water-soluble" aerosol from *d'Almeida et al.* [1991] are used for SO_4^{2-}(*nondust*)/NO_3^-(*nondust*)/NH_4^+/H_2O and OC. "Water-soluble" aerosol, as described in *d'Almeida et al.* [1991], includes sulfates, nitrates, as well as water-soluble organic aerosols. Refractive indices for BC and mineral dust aerosols are from *Liao et al.* [1999]. The size distributions of OC and mineral dust aerosols are those used in computing heterogeneous reactions. For BC, a lognormal distribution with a median radius of 0.0118 μm and a geometric standard deviation of 2.0 is assumed, with the density assumed to be 1.0 g cm^{-3} [*Haywood and Ramaswamy*, 1998]. We assume that wet SO_4^{2-}(*nondust*)/NO_3^-(*nondust*)/NH_4^+/H_2O aerosol has a lognormal distribution with a median radius of 0.09 μm and a geometric standard deviation of 2.0.

[23] Note that for the Fast-J calculation, we use the assumed size distribution for SO_4^{2-}(*nondust*)/NO_3^- (*nondust*)/NH_4^+/H_2O aerosol instead of the actual size distribution computed from chemical equilibrium at the local RH. This approximation reduces significantly the computing time needed for calculating aerosol phase functions. Small variations (less than 2%) were observed in predicted monthly mean concentrations of HNO_3 or O_3 when actual size distributions computed from chemical equilibrium were used in a sensitivity run.

2.4. Dry and Wet Deposition

[24] Calculation of dry deposition follows the procedure described by *Wang et al.* [1998]. Deposition velocities of all gas-phase species are determined following the resistance-in-series scheme of *Wesely* [1989]. The dry deposition velocity is inversely proportional to the sum of the aerodynamic resistance, sublayer resistance, and the surface resistance. Aerodynamic and sublayer resistances are calculated using local GCM surface fluxes of momentum and heat. Surface resistances for different species and for different surface types are based largely on the canopy model of *Wesely* [1989], with several improvements as described by *Wang et al.* [1998] to allow its extension to the global scale. Particle deposition velocities of SO_4^{2-}(*nondust*), NO_3^-(*nondust*) and NH_4^+ aerosols are calculated by using the scheme described for sulfate by *Koch et al.* [1999], which is not size-resolved. For all carbonaceous aerosols, a deposition velocity of 0.1 cm s^{-1} is assumed [*Liousse et al.*, 1996].

[25] The wet deposition scheme is that reported by *Koch et al.* [1999]. Wet deposition of dissolved tracers is treated separately for large-scale and convective clouds, following the GCM cloud schemes described by *Del Genio and Yao* [1993] and *Del Genio et al.* [1996]. Dissolved gases and aerosols are scavenged within and below precipitating clouds. The solubility of gases is determined by their effective Henry's law constants. For aerosols, the wet deposition scheme is not size dependent. Sulfate, ammonium, nitrate, and hydrophilic POA and BC aerosols are assumed to be fully soluble. Hydrophobic POA and BC are assumed to be insoluble. Following *Cooke et al.* [1999], we assume that ambient conversion of POA and BC from hydrophobic to hydrophilic occurs with an exponential decay lifetime of 1.15 days. For SOA, 80% is assumed to dissolve into clouds, consistent with findings of *Limbeck and Puxbaum* [2000]. The scavenged species return to the air if falling precipitation evaporates.

[26] We also consider scavenging of gas-phase HNO_3 by ice clouds. The GISS GCM distinguishes ice and water

Table 5. Global Annual Emissions

Species	Emission Rate
NO_x	
Fossil fuel combustion	20
Biomass burning	11
Soil (natural)	3.9
Soil (fertilizer)	0.5
Lightning	3.5
Aircraft	0.5
Stratosphere[a]	0.1
Total	40[b] (Tg N yr^{-1})
CO	
Fossil fuel combustion	390
Wood fuel combustion	130
Biomass burning	510
Total	1030[b] (Tg CO yr^{-1})
Isoprene	
Vegetation	550[b] (Tg C yr^{-1})
Ethane	
Industrial	6.2
Biomass burning	2.4
Total	8.6[b] (Tg C yr^{-1})
Propane[e]	
Industrial	6.7 (Tg C yr^{-1})
$\geq C_4$ alkanes	
Industrial	30[b] (Tg C yr^{-1})
$\geq C_3$ alkenes	
Industrial	10
Biogenic sources	16
Biomass burning	12
Total	38[b] (Tg C yr^{-1})
Acetone	
Biomass burning	9
Biogenic sources	14
Total	23[b] (Tg C yr^{-1})
SO_2	
GEIA industrial emissions	66.6
Biomass burning	2.3
Aircraft	0.1
Volcanoes (noneruptive)	3.5
Total	72.5[c] (Tg S yr^{-1})
DMS	
Oceanic source	10.7[c] (Tg S yr^{-1})
NH_3	
Domesticated animals	21.6
Fertilizers	9.0
Oceans	8.2
Biomass burning	5.9
Crops	3.6
Humans	2.6
Soils under natural vegetation	2.4
Other	0.4
Total	53.6[d] (Tg N yr^{-1})
Hydrocarbon I[f]	
α-Pinene	44
β-Pinene	29
Sabinene and terpenoid ketones	17
$^3\Delta$-Carene	5
Total	95 (Tg C yr^{-1})
Hydrocarbon II[f]	
Limonene	29(Tg C yr^{-1})
Hydrocarbon III[f]	
α- and γ-Terpinene	1.3
Terpinolene	2.5
Total	3.8 (Tg C yr^{-1})
Hydrocarbon IV[f]	
Myrcene	6
Terpenoid alcohols	23
Ocimene	3
Total	32 (Tg C yr^{-1})
Hydrocarbon V[f]	
Sesquiterpenes	13 (Tg C yr^{-1})
POA[g]	81 (Tg C yr^{-1})
BC[g,h]	12 (Tg C yr^{-1})

clouds by comparing the local layer temperature with a critical temperature [*Del Genio et al.*, 1996]. Ice water content IWC (g ice water/ m^3 air) carried in the GCM is used to calculate surface area density of ice A_s (cm^2/cm^3) by [*Lawrence and Crutzen*, 1998]

$$A_s = 2 \times 10^{-4} \mathrm{IWC}^{0.9} \tag{3}$$

Assuming an uptake efficiency r_e of 3×10^{14} molecules cm^{-2} for HNO_3 uptake on ice particles [*Abbatt*, 1997; *Zondlo et al.*, 1997], HNO_3 taken up by ice, U(kg/grid cell/time step), can be calculated by

$$U = \frac{10^{-3} r_e A_s M_{\mathrm{HNO_3}}}{N_A} V F_{\mathrm{cld}} \tag{4}$$

where $M_{\mathrm{HNO_3}}$ is the molecular weight of HNO_3, N_A is Avogadro's number, V (cm^3) is the volume of grid cell, and F_{cld} is the cloud fraction of the grid box. Ice crystals can fall out, evaporate, or persist as determined by GCM cloud scheme.

3. Emissions

[27] Estimated present-day global annual emissions are listed in Table 5. Emissions for NO_x, CO, isoprene, propane, alkanes, alkenes, and acetone follow those given by *Mickley et al.* [1999]. Sulfur emissions follow *Koch et al.* [1999]; anthropogenic emissions include seasonally varying fossil fuel combustion and industrial activities compiled by the Global Emissions of Inventory Activity (GEIA) [*Benkovitz et al.*, 1996], which is representative of 1985 emissions. Three percent of GEIA sulfur emissions are assumed to be sulfate, with the remainder of the emissions being SO_2. Other anthropogenic sources of SO_2 include biomass burning and aircraft emissions. Ammonia emissions are given by *Bouwman et al.* [1997], which take into account the major categories of domesticated animals, fertilizer application, and biomass burning.

[28] For carbonaceous aerosols, emissions of biomass and fossil fuel POA are based on the work of *Liousse et al.* [1996], and biomass and fossil fuel emissions of BC are taken from *Liousse et al.* [1996] and *Penner et al.* [1993], respectively. We assume that 80% of emitted BC and 50% of emitted POA are hydrophobic, and the remaining portions are hydrophilic [*Cooke et al.*, 1999]. Global monthly emission inventories of total monoterpenes and other reactive volatile organic compounds (ORVOCs) from biogenics are obtained from GEIA and are based on the work of *Guenther et al.* [1995]. To account for the diurnal variation in mono-

Notes to Table 5

[a]Downward transport of NO_x across the tropopause. This transport also supplies 0.38 Tg N $yr^{-1}$of HNO_3 globally.
[b]From *Mickley et al.* [1999].
[c]From *Koch et al.* [1999].
[d]From *Bouwman et al.* [1997].
[e]Included in the model as a direct emission of acetone; the yield of acetone from oxidation of propane is specified as 80% [*Singh et al.*, 1994].
[f]From *Guenther et al.* [1995] and *Griffin et al.* [1999a].
[g]From *Liousse et al.* [1996].
[h]From *Penner et al.* [1993].

terpene and ORVOCs emissions, instantaneous values are obtained by scaling monthly mean emissions to the cosine of the solar zenith angle. Contributions of individual compounds to total monoterpene and ORVOC emissions are reported in *Griffin et al.* [1999a]. Estimated annual emissions of SOA precursors, POA, and BC are also listed in Table 5.

4. Coupled Chemistry-Aerosol Simulations

[29] The focus of this work is to explore the implications of coupled interaction between gas-phase chemistry and aerosols. Simulations were performed with all components coupled on line, as described in section 2. The baseline simulation considers: (1) the effects of all aerosol classes (SO_4^{2-}(*nondust*)/NO_3^-(*nondust*)/NH_4^+/H_2O, POA, SOA, BC, and mineral dust) on photolysis rates; (2) in-cloud oxidation of SO_2 by both H_2O_2 and O_3; and (3) heterogeneous reactions on SO_4^{2-}(*nondust*)/NO_3^-(*nondust*)/NH_4^+/H_2O, OC, and mineral dust aerosol surfaces. All simulations were conducted for an 18-month period, with the first 6 months ignored for spin-up. One year of coupled simulation of global dynamics, gas-phase chemistry, and aerosols required about 9 days on one 250-MHz MIPS R10000 processor of a SGI Origin 2100 system.

[30] Simulation of gas-phase chemistry in the unified model follows that of O_3-NO_x-CO-CH_4-NMHC of *Mickley et al.* [1999], who simulated concentrations of gas-phase species in the same GISS GCM II', considered the heterogeneous reactions of N_2O_5, NO_3, NO_2, and HO_2 on sulfate surface by using off-line monthly average sulfate fields, but did not take into account the ice-scavenging of HNO_3. Since *Mickley et al.* [1999] extensively compared their model results with observations and the current predictions for the most part agree closely with those presented by *Mickley et al.* [1999], we do not repeat those comparisons with measurements in this work. We do focus, however, on the comparison of predicted gas-phase HNO_3 with measurements, since predicted HNO_3 concentrations by the unified model include scavenging of HNO_3 by ice clouds and aerosol interactions and are significantly different from those of *Mickley et al.* [1999]. Aerosol simulations in the unified model follow the sulfate simulation of *Koch et al.* [1999], the NO_3^- and NH_4^+ simulations of *Adams et al.* [1999], and the carbonaceous aerosol simulation of *Chung and Seinfeld* [2002]. *Adams et al.* [1999] have presented detailed predictions for SO_4^{2-}(*nondust*), NO_3^-(*nondust*) and NH_4^+ aerosols; based on off-line concentrations of gas-phase HNO_3, HO_2, OH, simulated concentrations were generally within a factor of two of observations. *Chung and Seinfeld* [2002] compared predicted OC and BC concentrations with measurements and found that both OC and BC concentrations tend to be underpredicted, often by about a factor of two. *Chung and Seinfeld* [2002] used off-line fields of OH, O_3 and NO_3 for SOA simulation while the current work uses predicted concentrations. By comparing aerosol predictions from the unified model with those of *Adams et al.* [1999] and *Chung and Seinfeld* [2002], we can examine the effect of full gas-phase/aerosol coupling.

4.1. Sulfur Dioxide

[31] Global SO_2 levels are determined mainly by emissions, dry deposition, dust uptake, and conversion to sulfate. Predicted annual, zonal average mixing ratios of SO_2 are shown in Figure 2. As expected, SO_2 exhibits its largest concentrations in the Northern Hemisphere, with annual and zonal average mixing ratios exceeding 1 ppbv in the middle latitudes near the surface. In the Southern Hemisphere, continental and oceanic emissions result in a small peak in the subtropics, and emissions of DMS from the oceans produce high latitude, lower tropospheric mixing ratios of about 50 pptv. A comparison of the present predictions to those of *Koch et al.* [1999] shows that in the Northern Hemisphere, current predictions are about 50 pptv lower, above ~650 mb in the middle latitudes and throughout the atmosphere at high latitudes. The difference is a result of the inclusion of both in-cloud oxidation of SO_2 by O_3 and uptake of SO_2 by mineral dust aerosol. *Koch et al.* [1999] showed that their simulation led to excessive SO_2 over North America and Europe, with larger biases occurring in the northernmost regions during wintertime. Inclusion of in-cloud oxidation of SO_2 by O_3 in the unified model improves the comparison with observations. In-cloud SO_2 oxidation by ozone is most important in winter when SO_2 emissions are high and H_2O_2 is limiting.

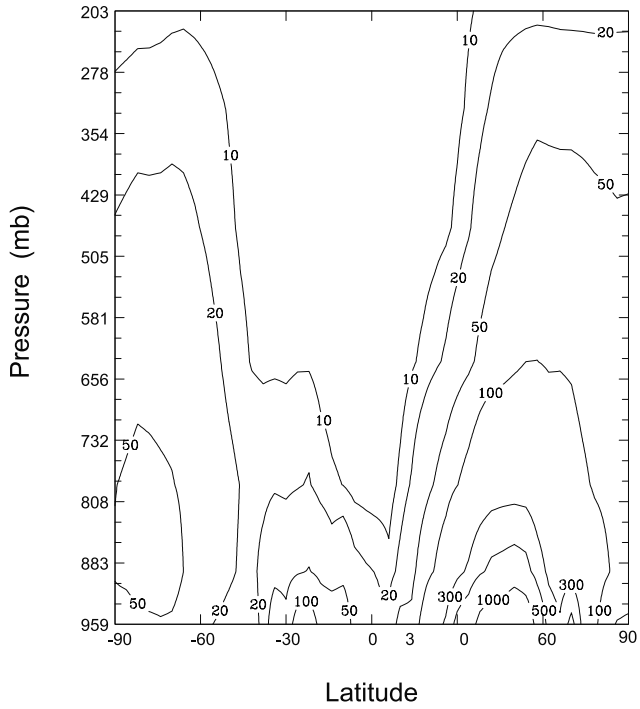

Figure 2. Predicted annual, zonal average SO_2 mixing ratios (pptv).

[32] Table 6 presents the yearly integrated sources and sinks for SO_2. The emissions follow those of *Koch et al.* [1999]. Loss of SO_2 through reaction with OH, 7.3 Tg S yr^{-1}, is less than the 13.1 Tg S yr^{-1} obtained by *Koch et al.* [1999] because of the inclusion of in-cloud SO_2 oxidation by O_3, and dust uptake. Oxidation by OH, H_2O_2, and O_3 accounts for 15, 65, and 20% of total SO_2 loss from oxidation pathways, respectively. The 20% loss through oxidation by O_3 agrees well with the result of *Roelofs et al.*

Table 6. Global Budget for SO_2

Sources (Tg S yr^{-1})	
Industrial emissions	64.9
Biomass burning	2.3
Volcanoes	3.4
DMS oxidation	12.4
Total sources	83.0
Sinks (Tg S yr^{-1})	
Oxidation	
by OH	7.3
by H_2O_2	31.8
by O_3	9.5
Dust uptake	3.9
Dry deposition	27.7
Wet deposition	2.8
Total sinks	83.0
Burden (Tg S)	0.26
Residence time (days)	1.1

[1998]. Dust uptake explains about 5% of the global sink of SO_2.

4.2. Sulfate

[33] Figure 3 shows predicted annual average SO_4^{2-}(*nondust*) and SO_4^{2-}(*dust*) mixing ratios near the surface and at 468 mb in the baseline simulation. The largest SO_4^{2-}(*nondust*) mixing ratios are predicted over the industrialized areas of Europe, North America, central and eastern Asia. Comparison of the annual averaged SO_4^{2-}(*nondust*) mixing ratios to those of *Adams et al.* [1999] shows that the coupled model predicts a 36% higher global mean mixing ratio of SO_4^{2-} near the surface but about 40% lower global mean mixing ratio in the middle to upper troposphere. The major factors leading to these differences are the inclusion of in-cloud oxidation of SO_2 by O_3 and dust uptake of SO_2. As a result of including in-cloud oxidation of SO_2 by O_3, predicted boundary layer SO_4^{2-}(*nondust*) mixing ratios exceed 1 ppbv in a large area extending from Europe to central Asia. And, since the oxidation of SO_2 by O_3 effectively allows SO_2 scavenging when H_2O_2 is titrated, less SO_2 is transported to higher layers to be subsequently oxidized to sulfate. Our simulation improves the wintertime agreement between predicted SO_4^{2-}(*nondust*) and observations. *Koch et al.* [1999] found that that their predicted SO_4^{2-}(*nondust*) was generally low in Europe during wintertime when in-cloud SO_2 oxidation by ozone is important. Mineral dust takes up SO_2 near the dust source regions but this process is not dominant in determining the global mean mixing ratio of SO_4^{2-}(*nondust*) in the surface layer. The global and annual average burden of SO_4^{2-}(*nondust*) predicted in the unified model is 1.64 Tg, which is 78% of that predicted by *Adams et al.* [1999].

[34] Concentrations of SO_4^{2} (*dust*) depend on the levels of dust aerosol, the alkalinity of the dust particles, the availability of SO_2, and relative humidity (section 2.2.1). The

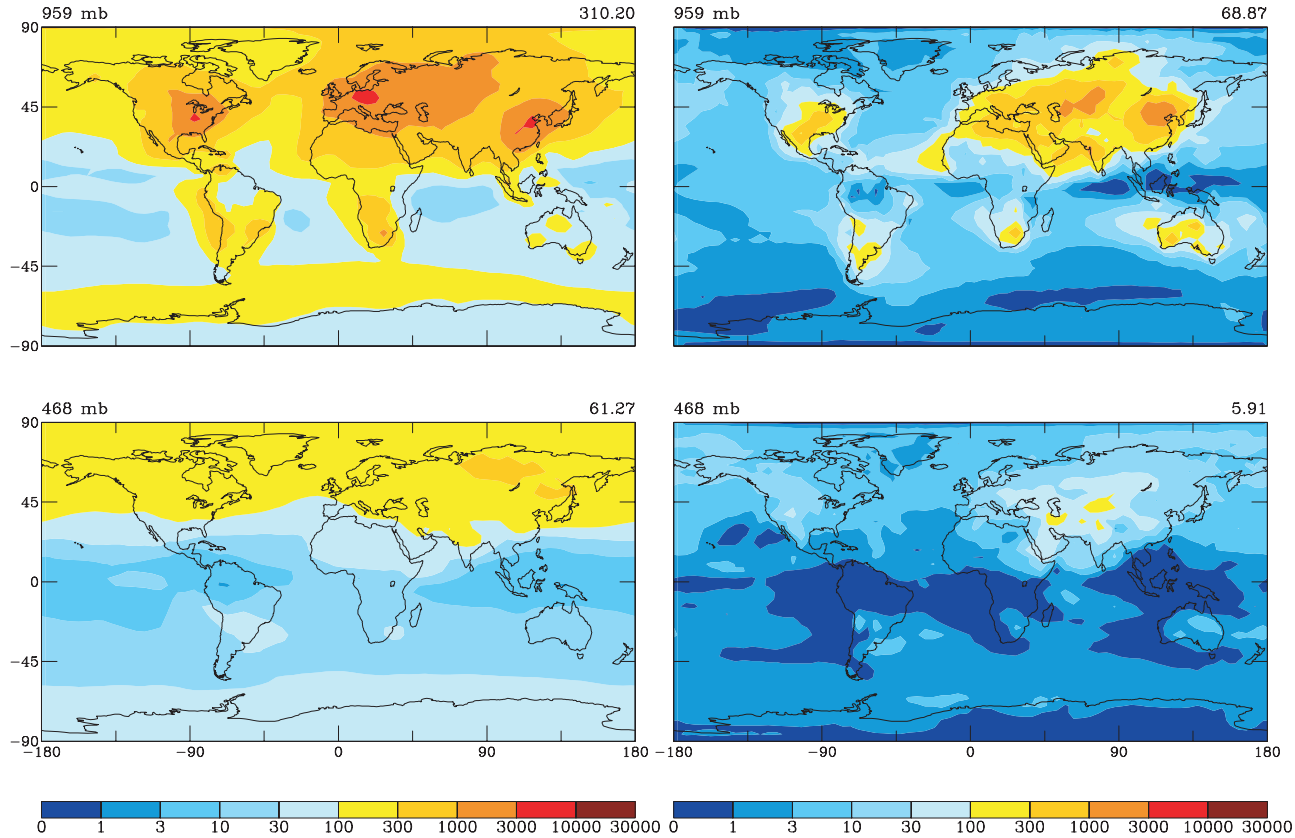

Figure 3. Predicted annual average mixing ratios (pptv) of SO_4^{2-}(*nondust*) (left column) and SO_4^{2-}(*dust*) (right column) near the surface and at 468 mb in the baseline simulation. See text for the definitions of SO_4^{2-}(*nondust*) and SO_4^{2-}(*dust*). Note that 1 μg m^{-3} SO_4^{2-} = 258 pptv SO_4^{2-} at 298 K and 1000 mb. Above each panel, the pressure level of the corresponding model layer is indicated, as is the average mixing ratio in that layer.

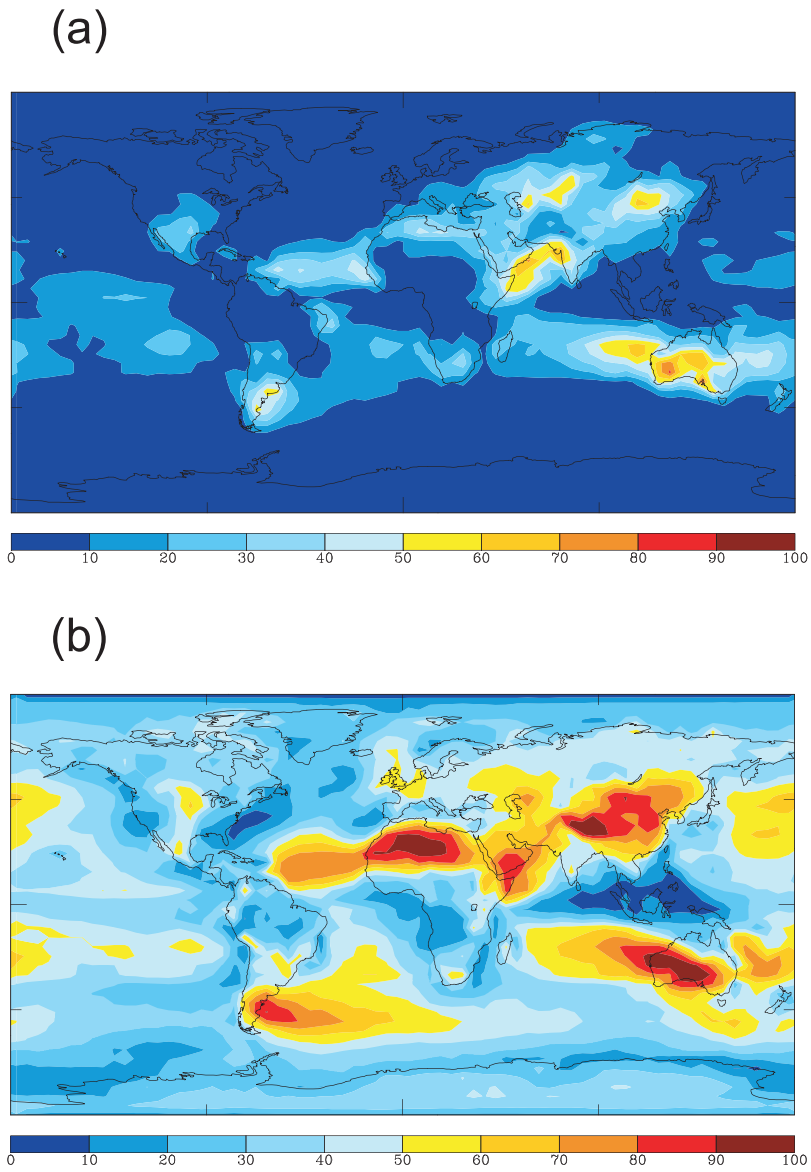

Figure 4. (a) Percent of total sulfate (SO_4^{2-}(*nondust*) + SO_4^{2-}(*dust*)) predicted to occur on mineral dust particles in the surface layer. (b) Percent of total nitrate (gas-phase HNO_3 + NO_3^-(*nondust*) + NO_3^-(*dust*)) occurring as nitrate aerosol (NO_3^-(*nondust*) + NO_3^-(*dust*)) in the surface layer.

largest SO_4^{2-}(*dust*) mixing ratios are predicted over central and northeast Asia.

[35] Figure 4a shows the predicted percent of annual mean total sulfate occurring on mineral dust at the surface layer. In the vicinity of dust source regions, such as central Asia, northeast Asia, Australia, and the coast of the northern Indian Ocean, more than 50% of total sulfate is predicted to be associated with mineral dust. Over a large portion of the Eurasian continent, 30–50% of total sulfate is predicted to be formed on dust particles. The fraction of sulfate on dust found here is in general agreement with that reported by *Dentener et al.* [1996]. *Dentener et al.* [1996] predicted a maximum located over Western Africa, while the current model predicts maxima over Australia and the northern Indian Ocean, corresponding to dust maxima predicted by *Tegen and Fung* [1994]. This difference might be caused either by the different meteorological fields or by the fact that *Dentener et al.* [1996] assumed the North African dust source was strongest in the Sahel region, whereas it was assumed to be strongest somewhat more northerly over Saudi Arabia/Horn of Africa in the study of *Tegen and Fung* [1994], from which the current mineral dust fields are taken.

4.3. Nitric Acid

[36] Predicted January and July HNO_3 mixing ratios near the surface and at 468 mb are shown in Figure 5. During daytime, nitric acid is produced by the reaction of NO_2 and OH and at night by hydrolysis of N_2O_5 on aerosol surfaces. Gas-phase HNO_3 is removed by reaction with OH, photolysis, wet and dry deposition, as well as by conversion to aerosol nitrate. Predicted Northern Hemisphere HNO_3 mixing ratios are higher in January than in July, reflecting less ventilation, loss of HNO_3 by photolysis, reaction with OH,

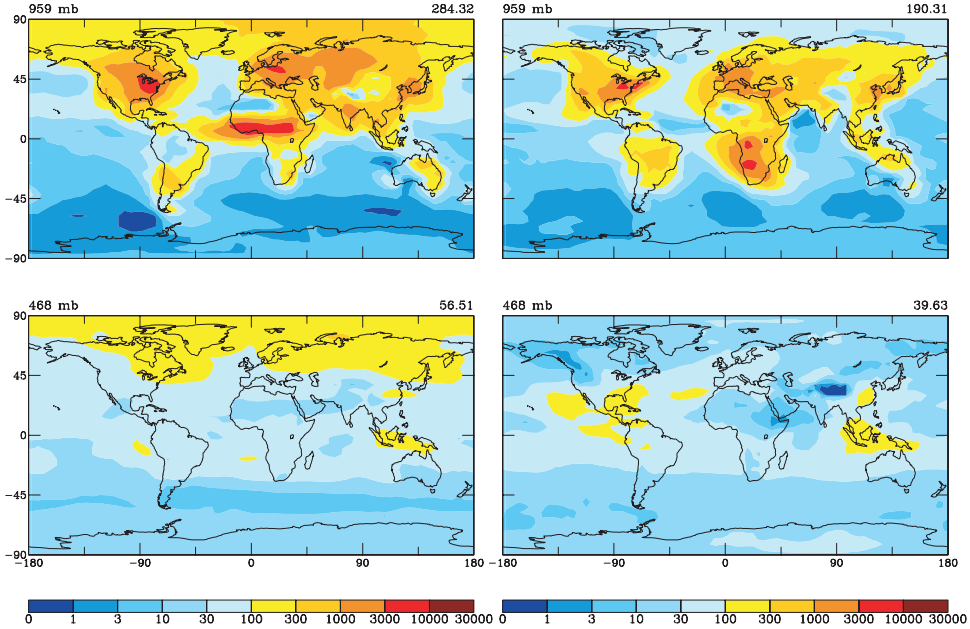

Figure 5. Predicted monthly mean gas-phase HNO_3 mixing ratios (pptv) near the surface and at 468 mb in January (left) and July (right) for the baseline simulation. Above each panel, the pressure level of the corresponding model layer in indicated, as in the average mixing ratio for that layer.

and deposition in winter. Largest predicted HNO_3 mixing ratios occur in the boundary layer of industrialized areas of Europe, North America, central and eastern Asia, and over biomass burning regions in the tropics. In these regions, calculated mixing ratios generally exceed 1 ppbv in the boundary layer. Over northern Africa and southern Asia, predicted HNO_3 mixing ratios at 468 mb are less than 30 pptv, considerably lower than those of about 200 pptv predicted by *Wang et al.* [1998]. This difference is a result of predicted uptake of HNO_3 by mineral dust aerosol (see section 4.4).

[37] Figure 6 compares predicted gas-phase HNO_3 profiles with aircraft measurements. As compared with *Wang et al.* [1998] and *Mickley et al.* [1999], calculated gas-phase HNO_3 profiles for the baseline case exhibit consistently closer agreement with observed profiles in almost all regions, especially the middle to upper troposphere. Although baseline upper troposphere HNO_3 mixing ratios are somewhat underestimated in locations such as the East China Sea, tropical South Atlantic, and Southern Africa, upper tropospheric HNO_3 is simulated well at all other locations. Previous overestimates of HNO_3 in the remote troposphere are greatly improved, with inclusion of wet deposition of HNO_3 on ice and uptake of HNO_3 by mineral dust aerosol. We will examine further the important processes that affect gas-phase HNO_3 concentrations in section 5.

4.4. Aerosol Nitrate

[38] In the absence of mineral dust aerosol, nitrate aerosol occurs mainly as neutralized ammonium nitrate, in an amount as determined by thermodynamic equilibrium. The presence of sulfate aerosol reduces nitrate formation because ammonia reacts preferentially with sulfate. Predicted annual average baseline mixing ratios of NO_3^-(*nondust*) and NO_3^-(*dust*) are shown in Figure 7. Boundary layer NO_3^-(*nondust*) mixing ratios exceeding 1 ppbv occur in Europe, eastern China, and the eastern United States. Locations and magnitudes of peak NO_3^-(*nondust*) mixing ratios are consistent with those of *Adams et al.* [1999]. NO_3^-(*dust*) mixing ratios exceeding 1 ppbv are predicted near the surface in dust source regions. On a global mean basis, NO_3^-(*dust*) formation is predicted to exceed NO_3^-(*nondust*) formation; near the surface, the predicted global average mixing ratio is 100 pptv for NO_3^-(*dust*) and 75 pptv for NO_3^-(*nondust*), while at 468 mb altitude, it is 41 pptv for NO_3^-(*dust*) and 18 pptv for NO_3^-(*nondust*).

[39] Figure 4b shows for the surface layer the percent of total nitrate (gas-phase $HNO_3 + NO_3^-$(*nondust*) + NO_3^-(*dust*)) predicted to occur as nitrate aerosol (NO_3^-(*nondust*) + NO_3^-(*dust*)). On an annual average basis, nitrate formed on mineral dust governs the distribution of high ratios of aerosol nitrate to total nitrate. Near dust source regions, more than 50% of total nitrate is in the aerosol phase, with values approaching 100% over the Sahara Desert, central Asia and Australia, where the formation of nitrate is limited by the availability of gas-phase HNO_3.

[40] A limitation of the nitrate simulation presented here is the lack of inclusion of sea salt. Since sea salt is known to take up gas-phase HNO_3 [*Tabazadeh et al.*, 1998], we expect that in the marine boundary layer some fraction of nitrate associated with ammonium and mineral dust, presented in Figure 7, may, in reality, be associated with sea salt.

4.5. Ammonia and Ammonium

[41] Ammonia is present in significant quantities in the atmosphere; it plays a key role in determining the pH of

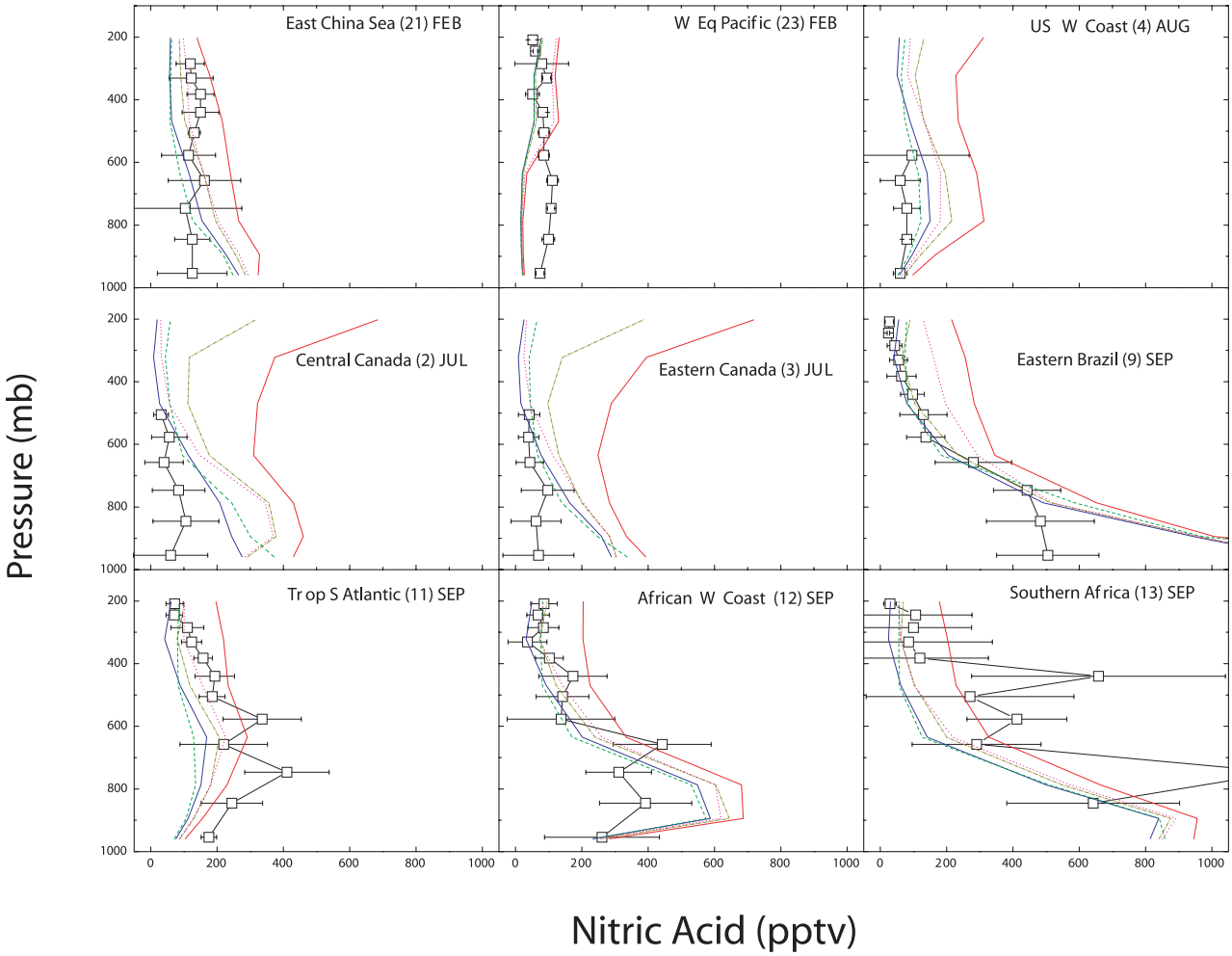

Figure 6. Comparison of observed vertical profiles of gas-phase HNO_3 with predicted profiles from different sensitivity studies. The region named in each panel is defined in *Wang et al.* [1998]. Open squares and solid lines are median observations, with standard deviations represented by solid horizontal bars. Model results are monthly mean predictions averaged over the grid cells encompassing each region. Lines include gas-phase HNO_3 predicted in the baseline simulation (blue), gas-phase HNO_3 from a sensitivity run with gas-aerosol partitioning removed from the baseline run (green), sensitivity run with dust uptake of HNO_3 removed (yellow), and sensitivity run with wet deposition of HNO_3 on ice removed (magenta). Gas-phase HNO_3 profiles predicted when all of the gas-aerosol partitioning, dust uptake of HNO_3, and wet deposition of HNO_3 on ice are removed from the baseline run are given by red lines.

cloud condensation nuclei and precipitation and is absorbed into the aerosol phase to form the ammonium ion, especially in the presence of sulfate.

[42] Predicted annual average mixing ratios of gas-phase ammonia near the surface and at 468 mb are shown by the left column of Figure 8. Locations and magnitudes of peak ammonia levels in India, China, Eastern Europe, and Brazil agree well with those of *Adams et al.* [1999]. Throughout the boundary layer, NH_3 concentrations are determined mainly by emissions and uptake by sulfate aerosol. The largest mixing ratios are predicted to exceed 3 ppbv, with continental mixing ratios generally exceeding 100 pptv. As a result of the strong emissions of NH_3 in India, NH_3 mixing ratios in this region still exceed 1 ppbv at 468 mb.

[43] Predicted annual average mixing ratios of particulate ammonium are shown by the right column of Figure 8. Highest ammonium mixing ratios, over 3 ppbv, are found in industrialized areas, such as the eastern United States, Europe, and China. Mixing ratios generally exceed 300 pptv over the continents. These results are also in good agreement with those of *Adams et al.* [1999].

4.6. Ozone

[44] Predicted monthly mean ozone mixing ratios (ppbv) near the surface and at 468 mb in January and July are shown in Figure 9 for the baseline simulation. Boundary layer ozone concentrations over industrial regions in the Northern Hemisphere in summer and over biomass burning regions in the tropics are in the range of 40–70 ppbv, levels that are consistent with those predicted by *Mickley et al.* [1999]. Predicted O_3 mixing ratios at 468 mb generally exceed those near the surface, as a result of emissions of NO_x from lightning and biomass burning, deep convection

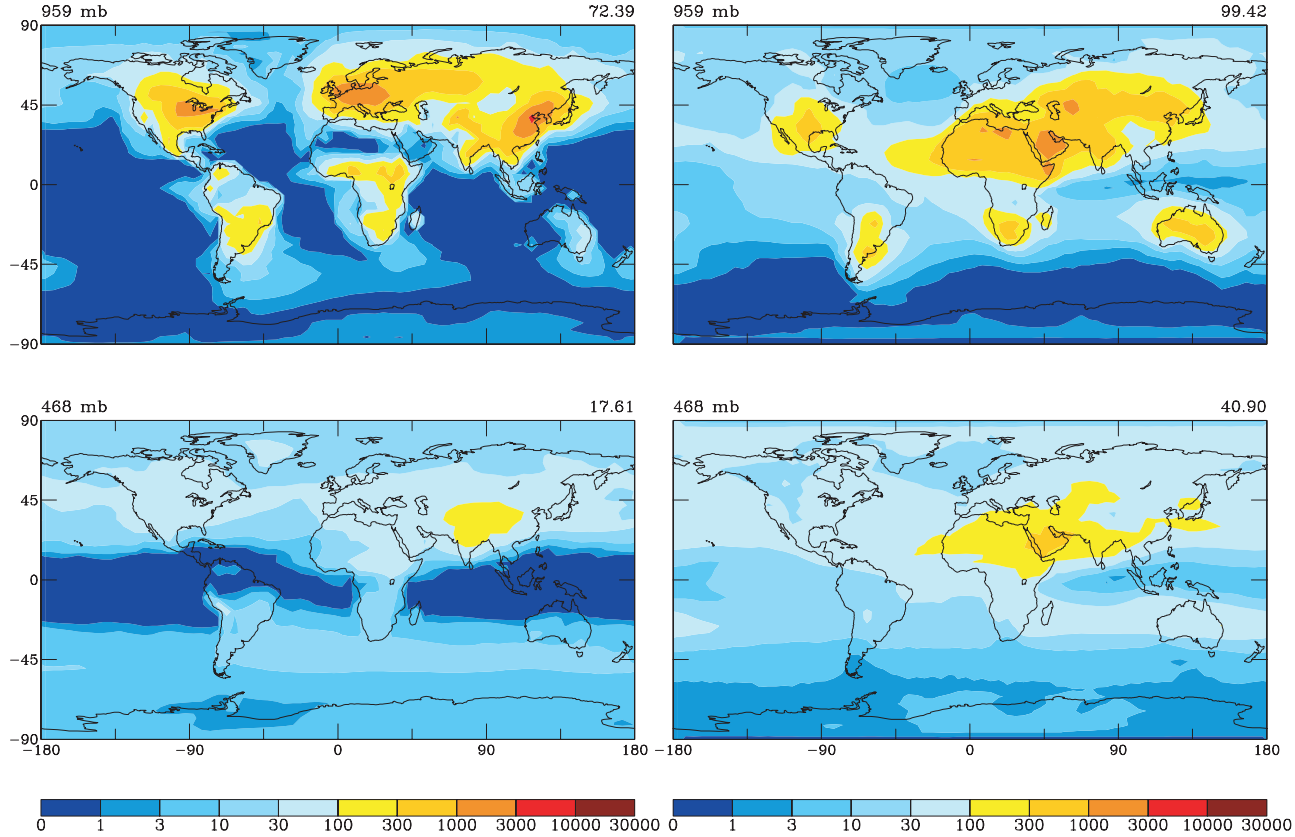

Figure 7. Predicted annual average mixing ratios (pptv) of NO_3^-(*nondust*) (left) and NO_3^-(*dust*) (right) near the surface and at 468 mb. Above each panel, the pressure level of the corresponding model layer is indicated, as is the average mixing ratio for that layer. Note that 1 μg m^{-3} NO_3^- = 400 pptv NO_3 at 298 K and 1000 mb.

from the continental boundary layer, transport from the stratosphere, as well as less dry deposition.

[45] A global budget of odd oxygen (O_x) is presented in Table 7. For the purpose of this budget, O_x is defined as the sum of O_3, O, NO_2, 2 × NO_3, HNO_4, 3 × N_2O_5, and the peroxyacylnitrates; ozone makes up over 99% of O_x globally. Calculated O_3 in situ chemical production and loss rates, 3761 and 3432 Tg yr^{-1}, respectively, are lower than the production rate of 4330 Tg yr^{-1} and the loss rate of 3960 Tg yr^{-1} obtained by *Mickley et al.* [1999] for the present-day atmosphere. The difference arises because the unified model considers additional NO_x removal by nitrate, ammonium, OC, and mineral dust aerosols as well as aerosol water. Mineral dust is predicted to take up 50 Tg O_3 per year.

4.7. Carbonaceous Aerosols

[46] Predicted annual global distributions of BC, POA, and SOA are shown in Figure 10 for the surface layer and 468 mb altitude. Distributions of BC and POA exhibit maxima near source regions over continents, where fossil fuel emissions are high. Elevated POA concentrations are also found in South America and Africa as a result of biomass burning. Predicted BC and POA concentrations are virtually identical to those predicted by *Chung and Seinfeld* [2002], including locations and magnitudes of the peak BC and POA levels in Europe, eastern China, North America, South America, and South Africa. Although spatial distributions of SOA are similar in both studies, the global mean concentration of SOA obtained when the gas and aerosol phases are fully coupled is about 20% higher than that of *Chung and Seinfeld* [2002] based on off-line OH, O_3, and NO_3.

5. Important Processes That Affect Gas-Phase HNO_3 Concentrations

[47] Observed gas-phase HNO_3 concentrations in the remote troposphere are generally lower than those predicted by tropospheric CTMs [*Hauglustaine et al.*, 1998; *Wang et al.*, 1998; *Lawrence and Crutzen*, 1998]. Phenomena that have not generally been included in global CTM simulations but have the potential to lead to lower predicted gas-phase HNO_3 levels include equilibrium gas-aerosol partitioning of HNO_3, uptake of HNO_3 by mineral dust aerosol, and scavenging of gas-phase HNO_3 by ice cloud particles (which can precipitate or evaporate before reaching the surface). To examine the relative importance of each of these three processes, we perform three sensitivity runs with each of the processes removed from the baseline simulation.

[48] Figure 11a shows the annual, zonal average mixing ratios (pptv) of gas-phase HNO_3 for the baseline simula-

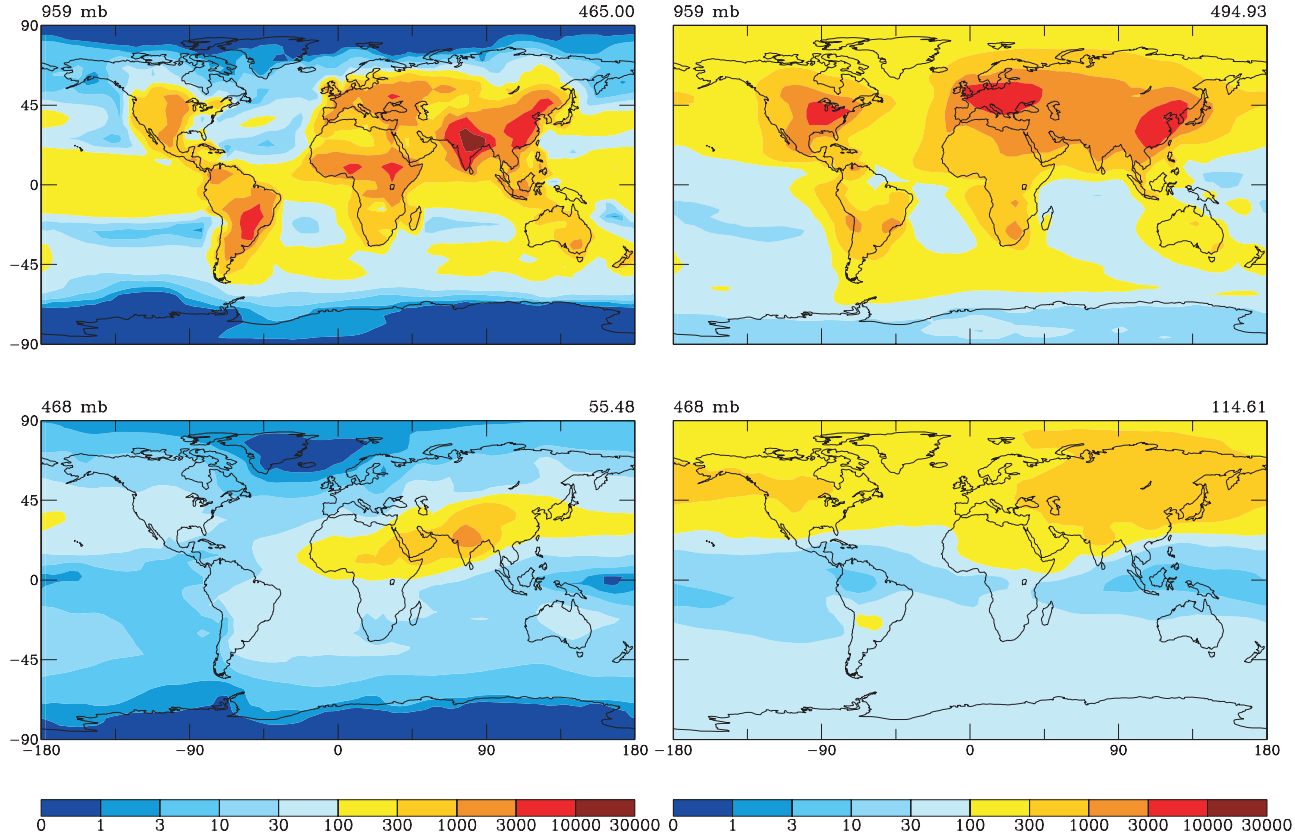

Figure 8. Predicted annual average mixing ratios (pptv) of gas-phase NH_3 (left column) and aerosol phase NH_4^+ (right column) near the surface and at 468 mb for baseline simulation. Note that 1 μg m^{-3} NH_3 = 1457 pptv NH_3 and 1 μg m^{-3} NH_4^+ = 1377 pptv NH_4^+ at 298 K and 1000 mb. Above each panel, the pressure level of the corresponding model layer is indicated, as is the average mixing ratio is that layer.

tion, while the other panels of Figure 11 present the ratio of the annual, zonal mean gas-phase HNO_3 mixing ratios obtained in each sensitivity run to the baseline values. Without equilibrium gas-aerosol partitioning (Figure 11b), predicted gas-phase HNO_3 mixing ratios are up to 30% larger near the surface and up to 60% larger in the upper troposphere. (Note the absolute concentrations of HNO_3 are small in the upper troposphere.) This is expected because particulate ammonium nitrate formation occurs mainly over polluted areas near the surface, and in the upper troposphere where SO_4^{2-}(*nondust*) concentrations are low and free NH_3 over strong NH_3 emissions is available for ammonium nitrate formation. What is not expected in the absence of gas-aerosol partitioning is a 10–20% decrease in predicted gas-phase HNO_3 in the middle troposphere over the subtropics of the Southern Hemisphere. This can be explained by the fact that the dry deposition of nitrate aerosol is much smaller than that of gas-phase HNO_3. Gas-phase HNO_3 does not survive long-distance transport, while, with gas-aerosol partitioning, nitrate transported to the remote troposphere may release gas-phase HNO_3 when conditions, such as temperature and relative humidity, change. The zonal mean reduction occurs only in the middle troposphere of the SH, because in other latitudes and altitudes, the decrease from transport is too small to offset the increase in gas-phase HNO_3 in the absence of equilibrium partitioning in polluted areas and in the upper troposphere.

[49] Without uptake of HNO_3 by mineral dust (Figure 11c), predicted gas-phase HNO_3 mixing ratios increase everywhere in the atmosphere compared with baseline values. While absolute increases in HNO_3 are about 100–150 pptv in the Northern Hemisphere (not shown), which are vertically fairly homogeneous, the highest percentage increase, about 300%, occurs near 300 mb in the middle to high latitudes of the Northern Hemisphere, and near 400 mb in the middle latitudes of the Southern Hemisphere. Significant dust uptake of HNO_3 generally occurs in areas with high HNO_3 and dust concentrations, but uptake of HNO_3 in the lower troposphere is affected by simultaneous uptake of SO_2, which is also important in determining dust alkalinity. With low SO_2 concentrations in the upper troposphere, uptake of HNO_3 can occur as long as the dust particles are alkaline, and HNO_3 is not limiting.

[50] Deposition of HNO_3 on ice also plays an important role in governing HNO_3 concentrations. Without deposition of HNO_3 on ice (Figure 11d), HNO_3 concentrations in the middle to upper troposphere increase significantly from baseline values.

[51] Dust uptake of HNO_3 and scavenging of HNO_3 by ice are predicted to be the most important factors that lower

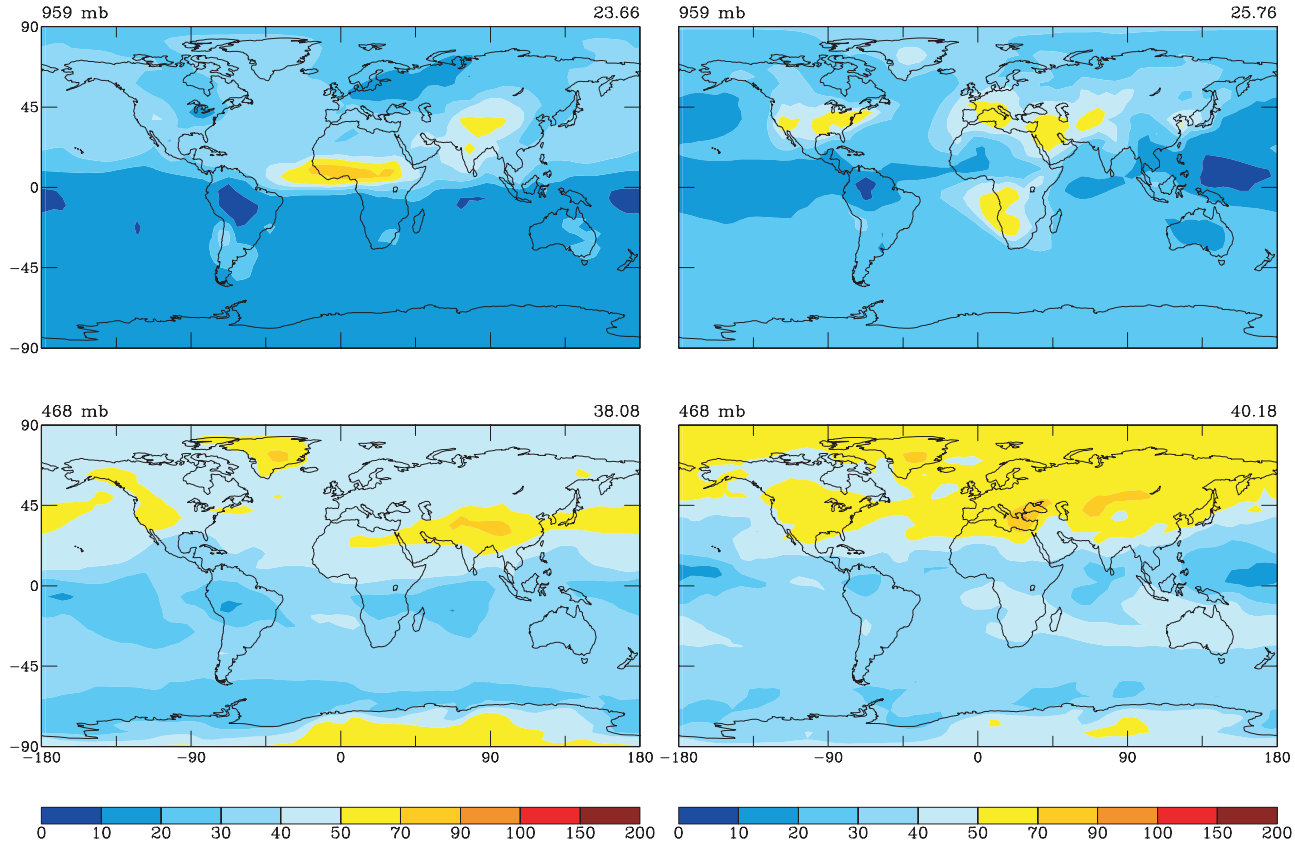

Figure 9. Predicted monthly mean ozone mixing ratios (ppbv) near the surface and at 468 mb in January (left) and July (right). Above each panel, the pressure level of the corresponding model layer is indicated, as is the average mixing ratio in that layer.

predicted gas-phase HNO_3 concentrations from those determined solely on the basis of gas-phase chemistry. Equilibrium gas-aerosol partitioning affects mainly HNO_3 concentrations in the polluted boundary layer and in the upper troposphere. These conclusions are also supported by Figure 6, which compares baseline HNO_3 levels to those from different sensitivity runs for different regions. Over US West Coast, central and eastern Canada, dust uptake is found to have dominant effect on gas-phase HNO_3 mixing ratios, since over these regions the HNO_3 mixing ratios increase significantly when dust uptake is removed from the baseline simulation. Over eastern Brazil and equatorial west Pacific, deposition on ice has dominant effect. Figure 6 also shows gas-phase HNO_3 profiles for a simulation with all of the dust uptake, equilibrium gas-aerosol partitioning, and wet deposition on ice removed from the baseline simulation. Differences between HNO_3 profiles demonstrate the importance of including all three processes discussed in simulations of gas-phase HNO_3.

6. Effect of Aerosols on Gas-Phase Chemistry Through Photolysis Rates

[52] To examine the effect of aerosols on gas-phase chemistry by altering photolysis rates, we perform a sensitivity run with all aerosols removed from the Fast-J scheme. Although urban scattering aerosols can alter photolysis rates by about 10–20% at small solar zenith angles [*Liao et al.*, 1999], the global effect of aerosols on HNO_3 and O_3 through altered photolysis rates is found to be small. At the surface layer, including aerosols in photolysis rate calculations leads to a maximum reduction of about 25 pptv in HNO_3 mixing ratios over central Africa, India, central and northeast Asia; this amount is to be compared with HNO_3 mixing ratios exceeding 1 ppbv in those regions. The largest reduction of about 1 ppbv in O_3 mixing ratios is found in regions with maximum HNO_3 reduction, but, as with HNO_3, the reduction is negligible compared with O_3 mixing ratios of 30–50 ppbv. Changes

Table 7. Global Budget for Tropospheric Ozone[a]

Sources (Tg O_3 yr^{-1})	
In situ chemical production	3761
Transport from stratosphere	401
Total sources	4162
Sinks (Tg O_3 yr^{-1})	
In situ chemical loss	3432
Dust uptake	50
Dry deposition	680
Total sinks	4162
Burden (Tg O_3)	318
Residence time (days)	28

[a]Budgets are for the odd oxygen family defined as the sum of O_3, O, NO_2, 2 × NO_3, HNO_4, 3 × N_2O_5, and the peroxyacylnitrates.

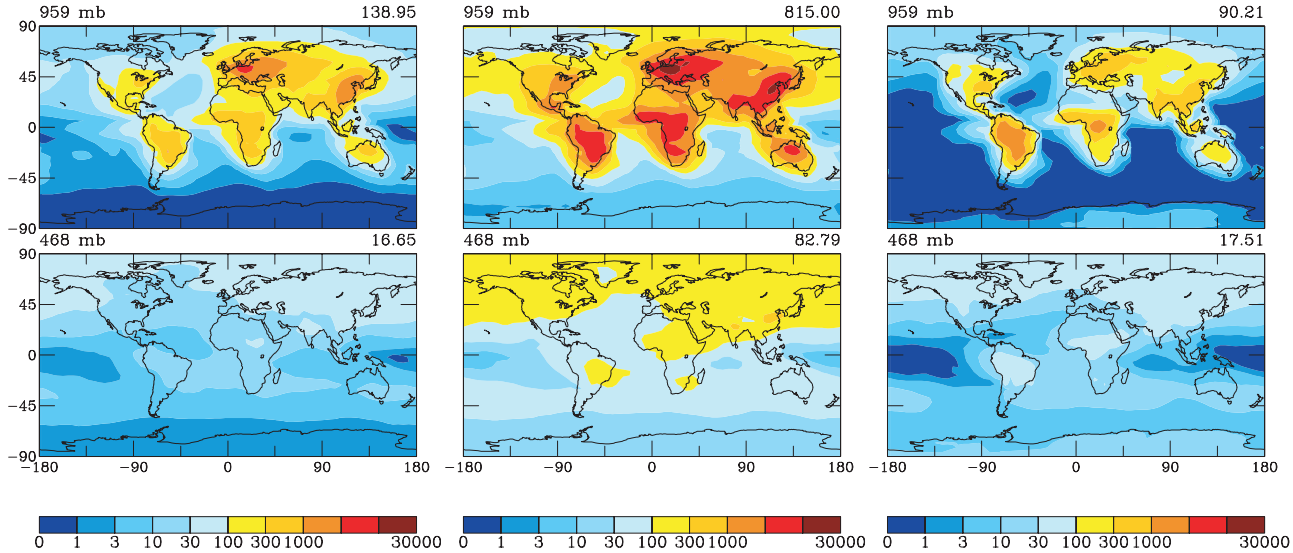

Figure 10. Predicted annual mean concentration (ng m^{-3}) near the surface and at 468 mb: (a) BC; (b) POA; and (c) SOA.

in HNO_3 and O_3 concentrations at 468 mb are even smaller than those at the surface. The small effects of aerosols found here agree with results of *Fiore et al.* [2002], which show that inclusion of aerosols in photolysis rate calculations changes monthly mean O_3 by less than 0.2 ppbv anywhere.

7. Effect of Heterogenous Reactions on Gas-Phase Chemistry and Aerosol Formation

7.1. Aerosol Surface Area

[53] Heterogeneous reactions occur on the surfaces of SO_4^{2-}(*nondust*)/NO_3^-(*nondust*)/NH_4^+/H_2O, OC, and mineral dust aerosols. In order to evaluate the role of each class of aerosol in heterogeneous chemistry, we calculate first the annual mean aerosol surface area as a column burden for (a) SO_4^{2-}(*nondust*)/NO_3^-(*nondust*)/NH_4^+/H_2O, (b) OC, and (c) mineral dust (Figure 12). Surface area concentrations of SO_4^{2-}(*nondust*)/NO_3^-(*nondust*)/NH_4^+/H_2O aerosol are much higher than those of OC and mineral dust; on a global mean basis, the surface areas of SO_4^{2-}(*nondust*)/NO_3^-(*nondust*)/NH_4^+/H_2O, OC, and mineral dust account for about 64, 22, and 14% of total aerosol surface area, respectively. It should be mentioned that dust surface fraction depends on assumed dust size distribution. *Dentener et al.* [1996] have pointed out that dust surface area may vary by a factor of 10 for a specified amount of mass.

7.2. Effects on Concentrations of Gas-Phase Species and Aerosols

[54] To determine the effects of heterogeneous reactions on gas-phase and aerosol chemistry, a sensitivity simulation is performed with all heterogeneous reactions (except in-cloud SO_2 oxidation) removed from the baseline simulation. Annual average NO_x, O_3, SO_4^{2-}(*nondust*), NO_3^-(*nondust*) and NH_4^+ concentrations in the absence of heterogeneous reactions can be compared with the baseline values. Figure 13 shows, for each species, the ratio of annual mean baseline mixing ratios (in the presence of aerosols) to those in the absence of heterogeneous reactions in the surface layer.

7.2.1. Gas-Phase Species

[55] The presence of aerosols leads to reduction in NO_x concentrations in the middle to high latitudes in both Northern and Southern Hemispheres (Figure 13a), with the maximum reduction of about 80% occurring at high latitudes of the NH. With high aerosol concentrations and low OH abundance at high latitudes of the NH, NO_x loss depends mainly on heterogeneous reactions. Since predicted aerosol concentrations in the SH are much smaller than those in the NH, the reduction of NO_x by heterogeneous reactions is found to be only about 10–30% in the middle to high latitudes of the SH. NO_x concentrations are not sensitive to heterogeneous reactions in the tropics, where the daytime reaction of NO_2 with OH is the most important NO_x removal mechanism. These effects of heterogeneous reactions on NO_x are similar to those found by *Dentener and Crutzen* [1993] in the SH and tropics. In the high latitudes of the NH, the simulation of *Dentener and Crutzen* [1993], which considered heterogeneous reactions of NO_3 and N_2O_5 on non-dust sulfate particles, predicted NO_x reductions of 80% from October to April and of 10–20% in summer. Present work predicts annual mean NO_x reductions of about 80% in the high latitudes of the NH, reflecting the effects of NO_3^-(*nondust*), ammonium, OC, and mineral dust aerosols.

[56] As a result of NO_x removal by aerosols and dust uptake of O_3, predicted baseline ozone concentrations are lower than those in the absence of heterogeneous reactions (Figure 13b). Ozone concentrations at NH high latitudes are predicted to be reduced by about 30% near the surface. Reactions on aerosols generally reduce O_3 concentrations by 10 to 15% in the SH. Of the two factors that cause O_3 reduction, dust uptake of O_3, and NO_x removal by SO_4^{2-}(*nondust*)/NO_3^-(*nondust*)/NH_4^+/H_2O, OC, and mineral dust, the latter is slightly more influential; the predicted global annual average O_3 burden would increase by 7% in

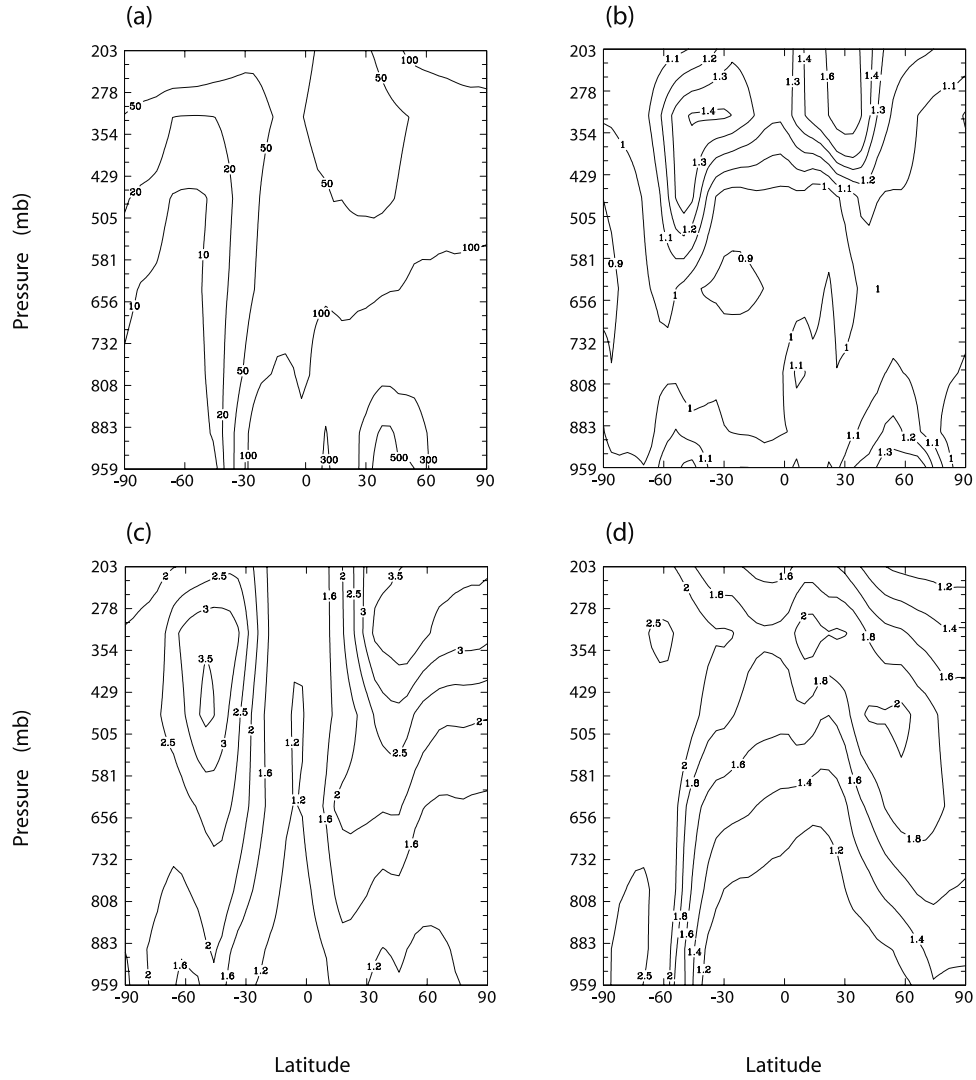

Figure 11. (a) Predicted annual, zonal average HNO_3 mixing ratios (pptv) for the baseline run; the remaining plots show the ratio of the annual, zonal mean mixing ratios of gas-phase HNO_3 (relative to the baseline simulation) considering: (b) gas-aerosol partitioning removed from the baseline simulation; (c) dust uptake of HNO_3 removed from the baseline simulation; and (d) wet deposition of HNO_3 on ice removed from the baseline simulation.

the absence of dust uptake and by 16% in the absence of both dust uptake and NO_x removal.

[57] Since the unified model considers O_3 reduction from both dust uptake of O_3 and NO_x removal on SO_4^{2-} (*nondust*)/NO_3^-(*nondust*)/NH_4^+/H_2O, OC, and mineral dust aerosols, ozone reductions obtained here cannot be compared directly with those predicted by *Dentener and Crutzen* [1993] or *Dentener et al.* [1996]. *Dentener and Crutzen* [1993] considered only O_3 reduction from heterogeneous reactions of NO_3 and N_2O_5 on non-dust sulfate particles, while *Dentener et al.* [1996] considered only O_3 reduction from dust uptake. However, in the high latitudes of the NH and SH, where dust concentrations are not high, O_3 reductions predicted in this work are in close agreement with those of *Dentener and Crutzen* [1993]. We obtain about 5–10% higher O_3 reductions in the high latitudes of the NH as a result of higher predicted NO_x removal there. Over Saudi Arabia/Horn of Africa, where the dust mass is the largest, O_3 reduction predicted in this work is about 15–20%, which is higher than the reduction of about 8% in same area obtained by *Dentener et al.* [1996]. This difference may result from the higher NO_x reduction predicted in the unified model and the different dust concentrations in different models.

7.2.2. Aerosols

[58] Heterogeneous reactions affect not only concentrations of gas-phase species but also those of aerosols. SO_4^{2-}(*nondust*) concentrations are reduced by dust uptake (Figure 13c). Near the surface, reductions of SO_4^{2-}(*nondust*) exceeding 20% occur near dust sources such as the Sahara Desert, central and eastern Asia, Australia, and southern South Africa.

[59] Changes in NO_3^-(*nondust*) mixing ratios near the surface (Figure 13d) reflect the changes in gas-phase

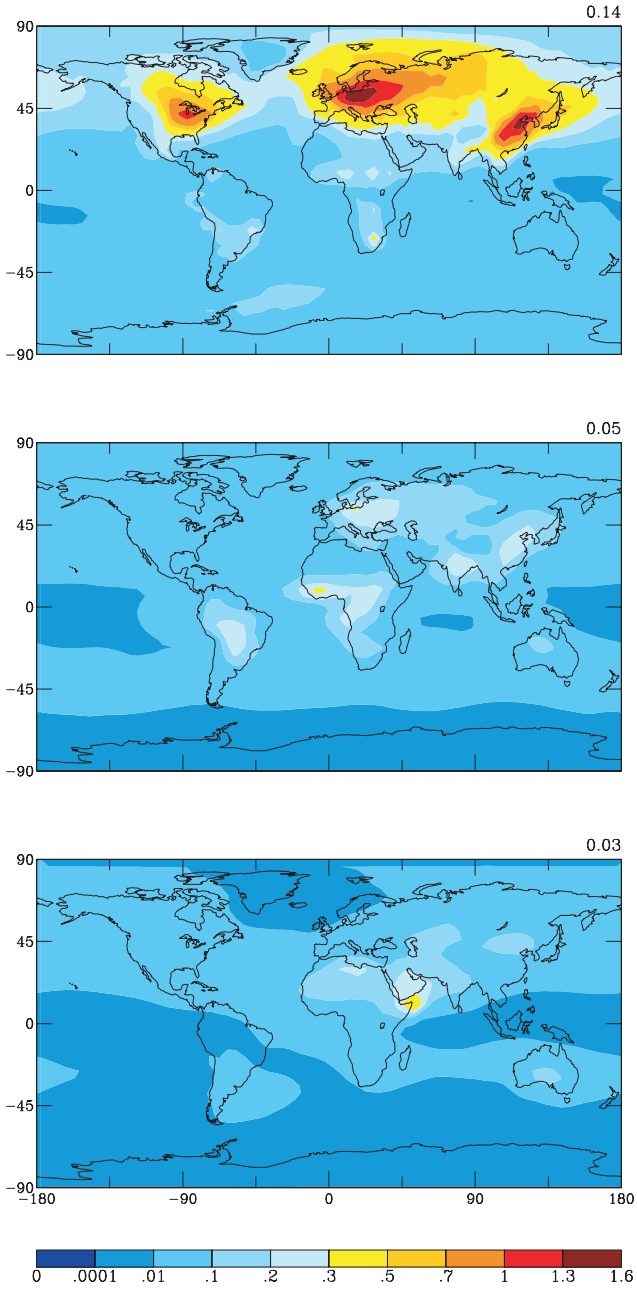

Figure 12. Annual mean column burden of aerosol surface area (m^2 aerosol/m^2) for: SO_4^{2-}(*nondust*)/NO_3^-(*nondust*)/NH_4^+(*nondust*)/H_2O (top panel); OC (middle panel); and mineral dust (bottom panel). Above each panel, the average value in that layer is indicated.

HNO_3 mixing ratios. As a result of hydrolysis of N_2O_5, the baseline run predicts higher gas-phase HNO_3 and hence a higher NO_3^-(*nondust*) concentrations over almost all continental areas except those near the dust sources.

[60] The changes in NH_4^+ (Figure 13e) depend on the changes in SO_4^{2-}(*nondust*) and NO_3^-(*nondust*). In the surface layer, NH_4^+ mixing ratios are reduced by dust uptake of SO_2 and HNO_3 near the dust source regions such as the Sahara Desert, the Arabian Peninsula, central Asia, southern South America, and Australia. Heterogeneous reactions increase surface NH_4^+ mixing ratios in the industrialized areas in Europe, South America, Africa, and eastern Asia, corresponding to the increase of NO_3^-(*nondust*) there. In these regions, NH_4^+ concentrations are increased by 10–20%.

7.3. Effects on Global and Annual Average Burdens

[61] To see the overall effects of heterogeneous reactions, we list in Table 8 the global and annual average burdens of some important species for the baseline run (with all the heterogeneous reactions) and the sensitivity run without heterogeneous reactions. Without heterogeneous reactions (dust uptake of SO_2), the burdens of SO_2 and SO_4^{2-}(*nondust*) are about 10% higher than those simulated with dust uptake, which has important implications for radiative forcing of sulfate. Compared with the baseline run, the predicted HNO_3 burden is 40% higher, and the O_3 burden increases by 16% in the absence of heterogeneous reactions. When compared with the baseline run, a higher NH_4^+ burden but lower NH_3 and NO_3^- (*nondust*) burdens in the absence of heterogeneous reactions indicate that the changes in the concentrations of these species are mainly affected by additional SO_4^- (*nondust*) formation.

[62] It should be noted that sulfate and nitrate aerosols associated with dust effectively may not change the radiative properties of dust particles. On each dust particle, masses of sulfate and nitrate account for only small fractions of dust mass.

7.4. Summary for Heterogeneous Reactions

[63] The presence of heterogeneous reactions generally reduces O_3 and SO_4^{2-}(*nondust*) concentrations, but they may locally increase or reduce NO_3^-(*nondust*) and NH_4^+ concentrations depending on whether dust is present. Dust uptake of SO_2 and HNO_3 leads to reduced concentrations of SO_4^{2-}(*nondust*), NO_3^-(*nondust*), and NH_4^+ near dust source regions, which can reduce radiative cooling by these aerosols there. Some climate models have considered the effect of heterogeneous reactions on O_3 concentrations, but the effects of heterogeneous reactions on aerosol concentrations are generally not included in estimates of aerosol radiative forcing. This issue requires more detailed study.

8. Sensitivity of Gas-Phase Chemistry and Aerosols to NO_x, NH_3, and Sulfur Emissions

[64] In a set of three sensitivity runs, total global emissions of each of NO_x, NH_3, and sulfur are increased by 50%. Table 8 shows the predicted baseline annual average global burden of the various gas-phase and aerosol species together with the burdens from the three sensitivity simulations. Burdens of gas-phase and aerosol phase species generally change nonlinearly with changes in emissions.

8.1. Sensitivity to NO_x Emissions

[65] Compared with the baseline run, a 50% increase in NO_x emissions increases O_3, HNO_3, NO_3^-(*nondust*), and NO_3^-(*dust*) burdens by 14, 37, 13, and 22%, respectively. As expected, more NH_4NO_3 formation occurs when more HNO_3 is available, resulting in a 13% increase in the NO_3^-(*nondust*) burden, a 5% increase in the NH_4^+ burden, and a 15% reduction in the NH_3 burden. More available

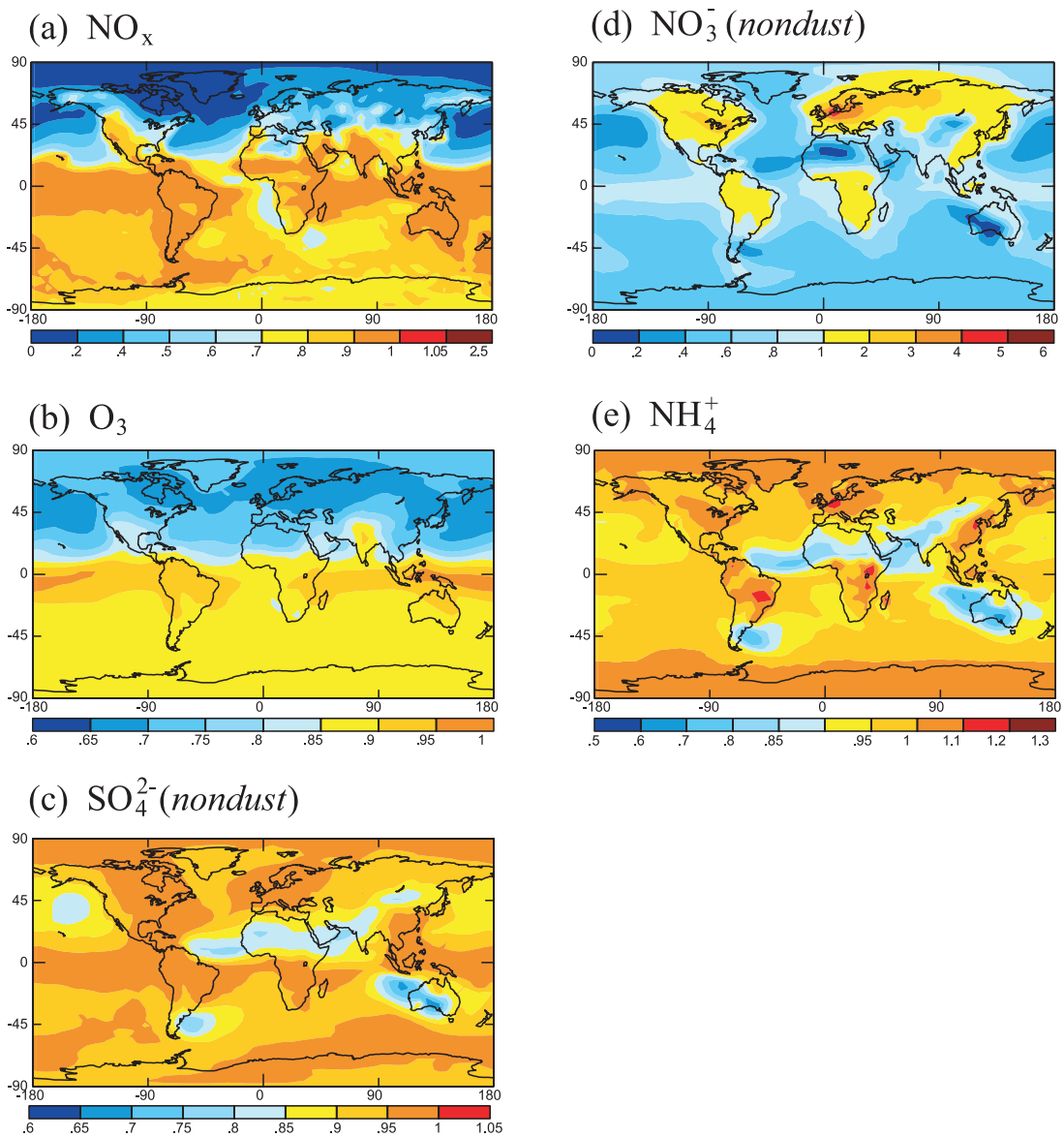

Figure 13. Ratio of annual mean mixing ratios calculated in the baseline run to those obtained in the absence of all heterogeneous reactions. For (a) NO_x, (b) O_3, (c) SO_4^{2-}(*nondust*), (d) NO_3^-(*nondust*), and (e) NH_4^+ in the GCM surface layer.

gas-phase HNO_3 also leads to 22% more nitrate formation on dust particles. Dust particles with $[Ca^{2+}] > [SO_4^{2-}(dust)] + 0.5[NO_3^-(dust)]$ can take up more HNO_3 when more HNO_3 is available, but, as a result, they take up less SO_2 once $[Ca^{2+}] > [SO_4^{2-}(dust)] + 0.5[NO_3^-(dust)]$ is satisfied; SO_4^{2-}(*dust*) burden is reduced by 21% in this sensitivity run. The increase in NO_x emissions also reduces SOA formation from OH and O_3 oxidation by 5%, while increasing that from NO_3 oxidation by 5%.

[66] An increase in NO_x emissions may influence in-cloud sulfate formation by aqueous oxidation of SO_2 by O_3 in several ways. The increase (or reduction) in O_3 concentrations can increase (or reduce) SO_4^{2-}(*nondust*), and the changed NO_3^-(*nondust*) and NH_4^+ can affect cloud pH. In this sensitivity run, reduction in SO_2 or the increase in SO_4^{2-}(*nondust*) occurs in areas with increased ozone, indicating that the changes in O_3 concentrations are more dominant in in-cloud sulfate formation than the changes in cloud pH. Near dust sources, since increased NO_x emissions lead to less SO_4^{2-}(*dust*) formation, more SO_2 is available for SO_4^{2-}(*nondust*) formation, and SO_4^{2-}(*nondust*) is predicted to increase by 30–100 pptv in these areas.

8.2. Sensitivity to NH_3 Emissions

[67] Compared with the baseline simulation, a 50% increase in NH_3 emissions increases the predicted burdens of NH_3, NH_4^+, and NO_3^-(*nondust*) by 95, 29, and 88%, respectively. With added NH_3 in the atmosphere, ammonium nitrate formation is limited by HNO_3; thus a 50% increase in NH_3 emissions is predicted to result in an increase in NH_4^+ burden by only 29%, leading to a significant increase in the burden of NH_3.

[68] Increasing NH_3 emission can also affect in-cloud sulfate formation through its effect on cloud pH. The burden

Table 8. Global and Annual Average Burdens (Tg) for the Baseline Case and Sensitivity Cases[a]

Species	Baseline Case	NO_x Emissions (+50%)	NH_3 Emissions (+50%)	Sulfur Emissions (+50%)	No Heterogeneous Reactions
SO_2	0.52	0.52 (0%)	0.50 (−4%)	0.89 (+71%)	0.56 (+8%)
SO_4^{2-}(*nondust*)	1.64	1.70 (+4%)	1.66 (+1%)	2.38 (+45%)	1.85 (+13%)
HNO_3	1.42	1.95 (+37%)	1.35 (−5%)	1.46 (+3%)	1.99 (+40%)
O_3	316	359 (+14%)	313 (−1%)	316 (0%)	367 (+16%)
H_2O_2	3.70	3.66 (−1%)	3.73 (+1%)	3.66 (−1%)	3.38 (−9%)
NH_3	0.20	0.17 (−15%)	0.39 (+95%)	0.14 (−30%)	0.16 (−20%)
NH_4^+	0.42	0.44 (+5%)	0.54 (+29%)	0.48 (+14%)	0.45 (+7%)
NO_3^-(*nondust*)	0.16	0.18 (+13%)	0.30 (+88%)	0.09 (−44%)	0.14 (−13%)
SO_4^{2-}(*dust*)	0.19	0.15 (−21%)	0.20 (+5%)	0.29 (+53%)	
NO_3^-(*dust*)	0.50	0.61 (+22%)	0.47 (−6%)	0.48 (−4%)	
BC	0.23	0.23 (0%)	0.23 (0%)	0.23 (0%)	0.23 (0%)
POA	1.24	1.24 (0%)	1.24 (0%)	1.24 (0%)	1.24 (0%)
SOA_{OH,O_3}[b]	0.18	0.17 (−5%)	0.18 (0%)	0.18 (0%)	0.17 (−5%)
SOA_{NO_3}[b]	0.042	0.044 (+5%)	0.042 (0%)	0.042 (0%)	0.044 (+5%)

[a]Numbers in parentheses are percentage changes compared with the baseline case.
[b]SOA_{OH,O_3} is SOA formation from OH and O_3 oxidation and SOA_{NO_3} is SOA formation from NO_3 oxidation.

of SO_2 is reduced by 4%. Some fraction of SO_2 reduction is caused by more conversion of SO_2 to SO_4^{2-}(*nondust*) in cloud droplets resulted from increased NH_4^+. And, because more HNO_3 exists as NH_4NO_3 when NH_3 emissions are increased, less gas-phase HNO_3 is available for dust uptake, and more SO_2 can be taken up by dust particles. The latter process also explains the 5% increase in SO_4^{2-}(*dust*) burden and the 6% reduction in NO_3^- burden.

8.3. Sensitivity to Sulfur Emissions

[69] With a 50% increase in sulfur emissions, burdens of SO_2 and SO_4^{2-}(*nondust*) are 71 and 45% higher than those in the baseline case, respectively. Higher sulfate burdens also lead to more ammonium sulfate formation; hence, the burden of NH_4^+ increases by 14%, whereas that of NH_3 decreases by 30%. As a consequence of increased ammonium sulfate, the formation of NH_4NO_3 is reduced, and the burden of NO_3^-(*nondust*) decreases by 44% as compared with the baseline simulation. Increasing sulfur emissions also affects the formation of sulfate and nitrate on dust particles. With more SO_2, dust particles are expected to take up less HNO_3 because of competition for alkalinity. Compared with the baseline run, the burden of SO_4^{2-}(*dust*) increases by 53%, while that of NO_3^-(*dust*) decreases by only 4%. The small amount of NO_3^-(*dust*) reduction can be explained as follows. As shown in Table 8, less ammonium nitrate formation leaves 3% more HNO_3 in the gas-phase available for dust uptake. And, in dust source regions, where relative humidity tends to be low, because of the assumed reaction probability dependence on RH, dust particles will take up HNO_3 preferentially. When these particles are transported to regions with RH exceeding 50%, some of the dust particles neutralized by nitrate are not available to uptake SO_2. Under such situations, the availability of more SO_2 affects the NO_3^-(*dust*) burden only marginally.

9. Summary and Conclusions

[70] We have developed a unified model for the study of chemistry-aerosol-climate interactions by incorporating a coupled tropospheric chemistry-aerosol simulation in the GISS GCM II'. The model includes a detailed simulation of tropospheric ozone-NO_x-hydrocarbon chemistry and prediction of sulfate/nitrate/ammonium, BC, primary organic carbon, and secondary organic carbon aerosols. The model takes into account the effects of all aerosol classes on photolysis rates, heterogeneous reactions of N_2O_5, NO_3, NO_2, and HO_2 on wetted aerosol surfaces, and uptake of SO_2, HNO_3, and O_3 by mineral dust. Although the current version of the unified model does not include a prognostic treatment of mineral dust aerosol, we include its effect on photolysis and heterogeneous processes by using three-dimensional off-line fields.

[71] We have compared our coupled simulation with the tropospheric chemistry simulation of *Mickley et al.* [1999], the SO_4^{2-}(*nondust*) simulation of *Koch et al.* [1999], the SO_4^{2-}(*nondust*)/NO_3^-(*nondust*)/NH_4^+ simulation of *Adams et al.* [1999], and the carbonaceous aerosol simulation of *Chung and Seinfeld* [2002]. Since we include in-cloud oxidation of SO_2 by O_3 and uptake of SO_2 by mineral dust, predicted upper tropospheric SO_2 concentrations are lower than those of *Koch et al.* [1999] in the middle and high latitudes of the Northern Hemisphere. For the same reason, predicted annual and global mean SO_4^{2-}(*nondust*) concentration is 36% higher near the surface but 40% lower in the middle troposphere compared with the values obtained by *Adams et al.* [1999]. Compared with previous studies, predicted gas-phase HNO_3 concentrations show closer agreement with measurements as a result of dust uptake of HNO_3 and scavenging of HNO_3 by ice.

[72] The unified model also simulates sulfate and nitrate aerosols that form on mineral dust particles. In the vicinity of dust source regions, more than 50% of total sulfate near the surface is predicted to be associated with mineral dust, which agrees with the results of *Dentener et al.* [1996]. On a global mean basis, based on currently available chemical understanding, nitrate aerosol formation on dust particles is predicted to exceed that resulting from ammonium nitrate aerosol formation.

[73] We have applied the unified model to investigate interactions between gas-phase chemistry and aerosols. The global effect of aerosols on gas-phase chemistry through altered photolysis rates is found to be small. Heterogeneous processes are shown to be important for both gas-phase species and aerosols. Although the surface area of mineral

dust is only a small fraction of total global aerosol surface area, mineral dust is predicted to play a significant role through uptake of O_3, SO_2, and HNO_3. It should be noted that calculations of heterogeneous reactions on aerosols are highly uncertain, especially those on mineral dust aerosol. The most uncertain factors in this study, reaction rates on mineral dust surface, dust size distribution, as well as dust alkalinity, deserve priority in both laboratory and modeling studies to further quantify the role of mineral dust in tropospheric chemistry.

[74] Interactions between gas-phase chemistry and aerosols are shown to be important in other aspects. For example, in-cloud sulfate formation is affected when O_3 concentration varies or when cloud droplet pH is influenced by aerosol formation. Sulfate and nitrate aerosol formation associated with mineral dust depends on the alkalinity of dust particles and availability of gas-phase HNO_3 and SO_2. Such processes interact with each other and lead to nonlinear changes in burdens of gas-phase species and aerosols when NO_x, ammonia, and sulfur emissions change. For example, an assumed across-the-board 50% increase in global NO_x emissions leads to predicted changes in burdens of HNO_3, O_3, SO_4^{2-}(*nondust*), NH_3, NH_4^+, NO_3^-(*nondust*), SO_4^{2-}(*dust*), NO_3^-(*dust*), SOA from OH and O_3 oxidation, and SOA from NO_3 oxidation by +37, +14, +4, −15, +5, +13, −21, +22, −5 and +5%, respectively. An increase in NH_3 emissions mainly influences burdens of NH_3, NH_4^+, and NO_3^-(*nondust*). A 50% increase in sulfur emissions significantly impacts SO_4^{2-}(*nondust*), SO_4^{2-}(*dust*), and ammonium nitrate formation, while it has small impact on HNO_3, O_3, and NO_3^-(*dust*) burdens.

[75] The capability for on-line simulation of ozone-NO_x-hydrocarbon and aerosols provides a platform for investigating the coupling among gas-phase chemistry, aerosols, and climate change.

[76] **Acknowledgments.** This work was supported by the National Aeronautics and Space Administration Earth Observing System Interdisciplinary Science program (NASA EOS-IDS). We also like to acknowledge the Center for Advanced Computing Research at Caltech for computing resources.

References

Abbatt, J. P. D., Interaction of HNO_3 with water-ice surfaces at temperatures of the free troposphere, *Geophy. Res. Lett.*, *24*, 1479–1482, 1997.

Adams, P. J., J. H. Seinfeld, and D. M. Koch, Global concentrations of tropospheric sulfate, nitrate, and ammonium aerosol simulated in a general circulation model, *J. Geophys. Res.*, *104*, 13,791–13,824, 1999.

Adams, P. J., J. H. Seinfeld, D. M. Koch, L. Mickley, and D. Jacob, General circulation model assessment of direct radiative forcing by the sulfate-nitrate-ammonium-water inorganic aerosol system, *J. Geophys. Res.*, *106*, 1097–1111, 2001.

Andreae, M. O., and P. J. Crutzen, Atmospheric aerosols: biogeochemical sources and role in atmospheric chemistry, *Science*, *276*, 1052–1058, 1997.

Atkinson, R., D. L. Baulch, R. A. Cox, R. F. Hampson Jr., J. A. Kerr, and J. Troe, Evaluated kinetic and photochemical data for tropospheric chemistry: Supplement IV, *Atmos. Environ.*, *26A*, 1187–1230, 1992.

Barth, M. C., P. J. Rasch, J. T. Kiehl, C. M. Benkovitz, and S. E. Schwartz, Sulfur chemistry in the National Center for Atmospheric Research Community Climate Model: Description, evaluation, features, and sensitivity to aqueous chemistry, *J. Geophys. Res.*, *105*, 1387–1415, 2000.

Benkovitz, C. M., M. T. Scholtz, J. Pacyna, L. Tarrason, J. Dignon, E. C. Voldner, P. A. Spiro, J. A. Logan, and T. E. Graedel, Global gridded inventories of anthropogenic emissions of sulfur and nitrogen, *J. Geophys. Res.*, *101*, 29,239–29,253, 1996.

Bouwman, A. F., D. S. Lee, W. A. H. Asman, F. J. Dentener, K. W. VanderHoek, and J. G. J. Olivier, A global high-resolution emission inventory for ammonia, *Global Biogeochem. Cycles*, *11*, 561–587, 1997.

Brasseur, G. P., D. A. Hauglustaine, S. Walters, P. J. Rasch, J.-F. Müller, C. Granier, and X. X. Tie, MOZART, a global chemical transport model for ozone and related chemical tracers, 1, Model description, *J. Geophys. Res.*, *103*, 28,265–28,289, 1998.

Castro, T., L. G. Ruizsuarez, J. C. Ruizsuarez, M. J. Molina, and M. Montero, Sensitivity analysis of a UV-radiation transfer model and experimental photolysis rates of NO_2 in the atmosphere of Mexico City, *Atmos. Environ.*, *31*, 609–620, 1997.

Chin, M., D. J. Jacob, G. M. Gardner, M. S. Foreman-Fowler, P. A. Spiro, and D. L. Savoie, A global three-dimensional model of tropospheric sulfate, *J. Geophys. Res.*, *101*, 18,667–18,690, 1996.

Chung, S. H., and J. H. Seinfeld, Global distribution and climate forcing of carbonaceous aerosols, *J. Geophys. Res.*, *104*, doi:10.1029/2001JD001397, in press, 2002.

Cooke, W. F., C. Liousse, H. Cachier, and J. Feichter, Construction of a 1° × 1° fossil fuel emission data set for carbonaceous aerosol and implementation and radiative impact in the ECHAM4 model, *J. Geophys. Res.*, *104*, 22,137–22,162, 1999.

d'Almeida, G. A., P. Koepke, and E. P. Shettle, *Atmospheric Aerosols: Global Climatology and Radiative Characteristics*, A. Deepak, Hampton, Va., 1991.

Del Genio, A. D., and M.-S. Yao, Efficient cumulus parameterization for long-term climate studies: The GISS scheme, in *The Representation of Cumulus Convection in Numerical Models*, *Monogr. 46*, edited by K. A. Emanuel and D. J. Raymond, pp. 181–184, AM. Meteorol. Soc., Boston, Mass., 1993.

Del Genio, A. D., M.-S. Yao, W. Kovari, and K. K.-W. Lo, A prognostic cloud water parameterization for global climate models, *J. Clim.*, *9*, 270–304, 1996.

Demerjian, K. L., K. L. Schere, and J. T. Peterson, Theoretical estimates of actinic (spherially integrated) flux and photolytic rate constants of atmospheric species in the lower troposphere, *Adv. Environ. Sci. Tech.*, *10*, 369–459, 1980.

DeMore, W. B., C. J. Howard, S. P. Sander, A. R. Ravishankara, D. M. Golden, C. E. Kolb, R. F. Hampson, M. J. Molina, and M. J. Kurylo, *Chemical Kinetics and Photochemical Data for Use in Stratospheric Modeling*, Jet Propulsion Lab., Pasadena, Calif., 1997.

Dentener, F. J., and P. J. Crutzen, Reaction of N_2O_5 on tropospheric aerosols: impact on the global distributions of NO_x, O_3, and OH, *J. Geophys. Res.*, *98*, 7149–7163, 1993.

Dentener, F. J., G. R. Carmichael, Y. Zhang, J. Lelieveld, and P. J. Crutzen, Role of mineral aerosol as a reactive surface in the global troposphere, *J. Geophys. Res.*, *101*, 22,869–22,889, 1996.

Dickerson, R. R., S. Kondragunta, G. Stenchikov, K. L. Civerolo, B. G. Doddridge, and B. N. Holben, The impact of aerosols on solar ultraviolet-radiation and photochemical smog, *Science*, *215*, 827–830, 1997.

Feichter, J., E. Kjellstrom, H. Rodhe, F. Dentener, J. Lelieveld, and G.-J. Roelofs, Simulation of the tropospheric sulfur cycle in a global climate model, *Atmos. Environ.*, *30*, 1693–1707, 1996.

Fenter, F. F., F. Caloz, and M. J. Rossi, Experimental evidence for efficient dry deposition of nitric acid on calcite, *Atmos. Environ.*, *29*, 3365–3372, 1995.

Fiore, A. M., D. J. Jacob, I. Bey, R. M. Yantosca, B. D. Field, A. C. Fusco, and J. G. Wilkinson, Background ozone over the United States in summer: Origin, trend, and contribution to pollution episodes, *J. Geophys. Res.*, *107*(D15), doi:10.1029/2001JD000982, 1643–1667, 2002.

Gay-Lacaux, C., and A. I. Modi, Precipitation chemistry in the Sahelian savanna of Niger, Africa, *J. Atmos. Chem.*, *30*, 319–343, 1998.

Galy-Lacaux, C., G. R. Carmichael, C. H. Song, J. P. Lacaux, H. Al Ourabi, and A. I. Modi, Heterogeneous processes involving nitrogenous compounds and Saharan dust inferred from measurements and model calculations, *J. Geophys. Res.*, *106*, 12,559–12,578, 2001.

Goodman, A. L., G. M. Underwood, and V. H. Grassian, A laboratory study of the heterogeneous reaction of nitric acid on calcium carbonate particles, *J. Geophys. Res.*, *105*, 29,053–29,064, 2000.

Goodman, A. L., E. T. Bernard, and V. H. Grassian, Spectroscopic study of nitric acid and water adsorption on oxide particles: Enhanced nitric acid uptake kinetics in the presence of adsorbed water, *J. Geophys. Res.*, *105*, 6443–6457, 2001.

Grassian, V. H., Heterogeneous uptake and reaction of nitrogen oxides and volatile organic compounds on the surface of atmospheric particles including oxides, carbonates, soot and mineral dust: implications for the chemical balance of the troposphere, *Int. Rev. Phys. Chem.*, *20*, 467–548, 2001.

Griffin, R. J., D. R. Cocker, J. H. Seinfeld, and D. Dabdub, Estimate of global atmospheric organic aerosol from oxidation of biogenic hydrocarbons, *Geophys. Res. Lett.*, *26*, 2721–2724, 1999a.

Griffin, R. J., D. R. Cocker, R. C. Flagan, and J. H. Seinfeld, Organic aerosol formation from the oxidation of biogenic hydrocarbons, *J. Geophys. Res.*, *104*, 3555–3567, 1999b.

Guenther, A., et al., A global model of natural volatile organic compound emissions, *J. Geophys. Res.*, *100*, 8873–8892, 1995.
Hanisch, F., and J. N. Crowley, Heterogeneous reactivity of gaseous nitric acid on Al_2O_3, $CaCO_3$, and atmospheric dust samples: A Knudsen cell study, *J. Phys. Chem. A*, *105*, 3096–3106, 2001.
Hansen, J. E., and L. D. Travis, Light scattering in planetary atmospheres, *Space Sci. Rev.*, *16*, 527–610, 1974.
Hansen, J., G. Russell, D. Rind, P. Stone, A. Lacis, S. Lebedeff, R. Ruedy, and L. Travis, Efficient three-dimensional global models for climate studies: Models I and II, *Mon. Weather Rev.*, *111*, 609–662, 1983.
Hansen, J., M. Sato, and R. Ruedy, Radiative forcing and climate response, *J. Geophys. Res.*, *102*, 6831–6864, 1997.
Hauglustaine, D. A., G. P. Brasseur, S. Walters, P. J. Rasch, J. F. Muller, L. K. Emmons, and C. A. Carroll, MOZART, a global chemical transport model for ozone and related chemical tracers, 2, Model results and evaluation, *J. Geophys. Res.*, *103*, 28,291–28,335, 1998.
Haywood, J. M., and V. Ramaswamy, Global sensitivity studies of the direct radiative forcing due to anthropogenic sulfate and black carbon aerosols, *J. Geophys. Res.*, *103*, 6043–6058, 1998.
Hoffmann, T., J. R. Odum, F. Bowman, D. Collins, D. Klockow, R. C. Flagan, and J. H. Seinfeld, Formation of organic aerosols from the oxidation of biogenic hydrocarbons, *J. Geophys. Res.*, *26*, 189–222, 1997.
Intergovernmental Panel on Climate Change (IPCC), *Climate Change 2001*, edited by J. T. Houghton et al., Cambridge Univ. Press, New York, 2001.
Jacob, D. J., Chemistry of OH in remote clouds and its role in the production of formic acid and peroxymonosulfate, *J. Geophys. Res.*, *91*, 9807–9826, 1986.
Jacob, D. J., Heterogeneous chemistry and tropospheric ozone, *Atmos. Environ.*, 2131–2159, 2000.
Jacobson, M. Z., Studying the effects of aerosols on vertical photolysis rate coefficient and temperature profiles over an urban airshed, *J. Geophys. Res.*, *103*, 10,593–10,604, 1998.
Jacobson, M. Z., and R. P. Turco, SMVGEAR – A sparse-matrix, vectorized GEAR code for atmospheric models, *Atmos. Environ.*, *28*, 273–284, 1994.
Johnson, C. E., Relative roles of climate and emissions changes on future tropospheric oxidant concentrations, *Geophys. Res.*, *104*, 18,631–18,645, 1999.
Kjellstrom, E., A three-dimensional global model study of carbonyl sulfide in the troposphere and the lower stratosphere, *J. Atmos. Chem.*, *29*, 151–177, 1998.
Koch, D. M., Transport and direct radiative forcing of carbonaceous and sulfate aerosols in the GISS GCM, *J. Geophys. Res.*, *106*, 20,311–20,332, 2001.
Koch, D. M., D. Jacob, I. Tegen, D. Rind, and M. Chin, Tropospheric sulfur simulation and sulfate direct radiative forcing in the Goddard Institute for Space Studies general circulation model, *J. Geophys. Res.*, *104*, 23,799–23,822, 1999.
Landgraf, J., and P. J. Crutzen, An efficient method for online calculations of photolysis and heating rates, *J. Atmos. Sci.*, *55*, 863–878, 1998.
Lantz, K. O., R. E. Shetter, C. A. Cantrell, S. J. Flocke, J. G. Calvert, and S. Madronich, Theoretical, actinometric, and radiometric determinations of the photolysis rate coefficient of NO_2 during the Mauna Loa observatory photochemistry experiment 2, *J. Geophys. Res.*, *101*, 14,613–14,629, 1996.
Lawrence, M. G., and P. J. Crutzen, The impact of cloud particle gravitational settling on soluble trace gas distributions, *Tellus, Ser. B*, *50*, 263–289, 1998.
Lelieveld, J., G.-J. Roelofs, J. Feichter, and H. Rodhe, Terrestrial sources and distribution of atmospheric sulphur, *Philos. Trans. R. Soc. London*, *352*, 149–157, 1997.
Liao, H., Y. L. Yung, and J. H. Seinfeld, Effects of aerosols on tropospheric photolysis rates in clear and cloudy atmospheres, *J. Geophys. Res.*, *104*, 23,697–23,707, 1999.
Limbeck, A., and H. Puxbaum, Dependence of in-cloud scavenging of polar organic aerosol compounds on the water solubility, *J. Geophys. Res.*, *105*, 19,857–19,867, 2000.
Liousse, C., J. E. Penner, C. Chuang, J. J. Walton, H. Eddleman, and H. Cachier, A global three-dimensional model study of carbonaceous aerosols, *J. Geophys. Res.*, *101*, 19,411–19,432, 1996.
Lohmann, U., K. von Salzen, N. McFarlane, H. G. Leighton, and J. Feichter, Tropospheric sulfur cycle in the Canadian general circulation model, *J. Geophys. Res.*, *104*, 26,833–26,858, 1999.
Maahs, H. G., Sulfur dioxide/water euilibrium between 0° and 50°C: An examination of data at low concentrations, in *Heterogeneous Atmospheric Chemistry, Geophys. Monogr. Ser.*, vol. 26, edited by D. R. Schryer, p. 273, AGU, Washington, D. C., 1982.
McPeters, R., Ozone profile comparisons, in *The Atmospheric Effects of Stratospheric Aircraft: Report of the 1992 Models and Measurement Workshop*, edited by E. E. Remsberg and M. J. Prather, pp. D1–D37, NASA Ref. Publ. 1292, 1993.
Mickley, L. J., P. Murti, D. Jacob, J. Logan, and D. Rind, Radiative forcing from tropospheric ozone calculated with a unified chemistry-climate model, *J. Geophys. Res.*, *104*, 30,153–30,172, 1999.
Mishchenko, M. I., W. B. Rossow, A. Macke, and A. A. Lacis, Sensitivity of cirrus cloud albedo, bidirectional reflectance and optical thickness retrieval accuracy to ice particle shape, *J. Geophys. Res.*, *101*, 16,973–16,985, 1996.
National Bureau of Standards, Selected values of chemical thermodynamic properties, 1, *Tech. Note 270-1*, Gaithersburg, Md., 1965.
National Research Council, *Global Air Quality: An Imperative for Long-Term Observation Strategies*, Natl Acad. Press, Washington, D. C., 2001.
Nenes, A., C. Pilinis, and S. N. Pandis, Isorropia: A new thermodynamic equilibrium model for multiphase multicomponent inorganic aerosols, *Aquat. Geochem.*, *4*, 123–152, 1998.
Pankow, J. F., An absorption model of gas/particle partitioning of organic compounds in the atmosphere, *Atmos. Environ.*, *28*, 185–188, 1994a.
Pankow, J. F., An absorption model of gas/particle partitioning involved in the formation of secondary organic aerosol, *Atmos. Environ.*, *28*, 189–193, 1994b.
Penner, J. E., H. Eddleman, and T. Novakov, Towards the development of a global inventory of black carbon emissions, *Atmos. Environ.*, *27A*, 1277–1295, 1993.
Rind, D., and J. Lerner, The use of on-line tracers as a diagnostic tool in general circulation model development, 1, Horizontal and vertical transport in the troposphere, *J. Geophys. Res.*, *101*, 12,667–12,683, 1996.
Rind, D., J. Lerner, K. Shah, and R. Suozzo, Use of on-line tracers as a diagnostic tool in general circulation model development, 2, Transport between the troposphere and stratosphere, *J. Geophys. Res.*, *104*, 9151–9167, 1999.
Roelofs, G.-J., and J. Lelieveld, Distribution and budget of O_3 in the troposphere calculated with a chemistry general circulation model, *J. Geophys. Res.*, *100*, 20,983–20,998, 1995.
Roelofs, G.-J., and J. Lelieveld, Tropospheric ozone simulation with a chemistry-general circulation model: Influence of higher hydrocarbon chemistry, *J. Geophys. Res.*, *105*, 22,697–22,712, 2000.
Roelofs, G.-J., J. Lelieveld, and R. van Dorland, A three-dimensional chemistry/general circulation model simulation of anthropogenically derived ozone in the troposphere and its radiative forcing, *J. Geophys. Res.*, *102*, 23,389–23,401, 1997.
Roelofs, G.-J., J. Lelieveld, and L. Ganzeveld, Simulation of global sulfate distribution and the influence on effective cloud drop radii with a coupled photochemistry sulfur cycle model, *Tellus, Ser. B*, *50*, 224–242, 1998.
Ruggaber, A., R. Dlugir, and T. Nakajima, Modeling radiation quantities and photolysis frequencies in the atmosphere, *J. Atmos. Chem.*, *18*, 171–210, 1994.
Schwartz, S. E., Mass-transport considerations pertinent to aqueous-phase reactions of gases in liquid-water clouds, in *Chemistry of Multiphase Atmospheric Systems*, edited by W. Jaechske, pp. 415–471, Springer-Verlag, New York, 1986.
Seinfeld, J. H., and S. N. Pandis, *Atmospheric Chemistry and Physics*, John Wiley, New York, 1998.
Shindell, D. T., J. L. Grenfell, D. Rind, V. Grewe, and C. Price, Chemistry-climate interactions in the Goddard Institute for Space Studies general circulation model, 1, Tropospheric chemistry model description and evaluation, *J. Geophys. Res.*, *106*, 8047–8075, 2001.
Singh, H. B., D. Ohara, D. Herlth, W. Sachse, D. R. Blake, J. D. Bradshaw, M. Kanakidou, and P. J. Crutzen, Acetone in the atmosphere: Distribution, sources, and sinks, *J. Geophys. Res.*, *99*, 1805–1819, 1994.
Sinha, A., and R. Toumi, Tropospheric ozone, lightning, and climate change, *J. Geophys. Res.*, *102*, 10,667–10,672, 1997.
Song, C. H., and G. R. Carmichael, A three-dimensional modeling investigation of the evolution processes of dust and sea-salt particles in East Asia, *J. Geophys. Res.*, *106*, 18,131–18,154, 2001.
Tabazadeh, A., M. Z. Jacobson, H. B. Singh, O. B. Toon, J. S. Linn, R. B. Chatfield, A. N. Thakur, R. W. Talbot, and J. E. Dibb, Nitric acid scavenging by mineral and biomass burning aerosols, *Geophys. Res. Lett.*, *25*, 4185–4188, 1998.
Tang, I. N., Thermodynamic and optical properties of mixed-salt aerosols of atmospheric importance, *J. Geophys. Res.*, *102*, 1883–1893, 1997.
Tegen, I., and I. Fung, Modeling of mineral dust in the atmosphere; sources, transport, and optical thickness, *J. Geophys. Res.*, *99*, 22,897–22,914, 1994.
Tegen, I., and I. Fung, Contribution to the atmospheric mineral aerosol load from land surface modification, *J. Geophys. Res.*, *100*, 18,707–18,726, 1995.
Tegen, I., and R. Miller, A general circulation model study on the interannual variability of soil dust aerosol, *J. Geophys. Res.*, *103*, 25,975–25,995, 1998.

Toumi, R., J. D. Haigh, and K. S. Law, A tropospheric ozone-lightning climate feedback, *Geophys. Res. Lett.*, *23*, 1037–1040, 1996.

Underwood, G. M., P. Li, H. Al-Abadleh, and V. H. Grassian, A Knudsen cell study of the heterogeneous reactivity of nitric acid on oxide and mineral dust particles, *J. Phys. Chem.*, 6609–6620, 2001.

Wang, Y., D. J. Jacob, and J. A. Logan, Global simulation of tropospheric O_3-NO_x-hydrocarbon chemistry, 1, Model formulation, *J. Geophys. Res.*, *103*, 10,713–10,725, 1998.

Wesely, M. L., Parameterization of surface resistances to gaseous dry deposition in regional-scale numerical models, *Atmos. Environ.*, *23*, 1293–1304, 1989.

Wild, O., X. Zhu, and M. J. Prather, Fast-J: Accurate simulation of in- and below-cloud photolysis in tropospheric chemical models, *J. Atmos. Chem.*, *37*, 245–282, 2000.

Woodward, S., Modeling the atmospheric life cycle and radiative impact of mineral dust in the Hadley Centre climate model, *J. Geophys. Res.*, *106*, 18,155–18,166, 2001.

Yienger, J. J., and H. Levy, Empirical-model of global soil-biogenic NO_x emissions, *J. Geophys. Res.*, *100*, 11,447–11,464, 1995.

Zhang, Y., and G. R. Carmichael, The role of mineral aerosol in tropospheric chemistry in East Asia – A model study, *J. Appl. Meteorol.*, *38*, 353–366, 1999.

Zondlo, M. A., S. B. Barone, and M. A. Tolbert, Uptake of HNO33 on ice under upper tropospheric conditions, *Geophy. Res. Lett.*, *24*, 1391–1394, 1997.

P. J. Adams, S. H. Chung, H. Liao, and J. H. Seinfeld, Division of Engineering and Applied Science and Department of Chemical Engineering, California Institute of Technology, Pasadena, CA 91125, USA. (petera@its.caltech.edu; hong@its.caltech.edu; seinfeld@caltech.edu)

D. J. Jacob and L. J. Mickley, Department of Earth and Planetary Sciences and Division of Engineering and Applied Sciences, Harvard University, Cambridge, MA 02138, USA. (djj@io.harvard.edu; ljm@io.harvard.edu)